

GEOSPHERE, v. 15, no. 5

<https://doi.org/10.1130/GES02088.1>

14 figures; 4 tables; 1 supplemental file

CORRESPONDENCE: sangster@nevada.unr.edu

CITATION: Angster, S.J., Wesnousky, S.G., Figueiredo, P.M., Owen, L.A., and Hammer, S.J., 2019, Late Quaternary slip rates for faults of the central Walker Lane (Nevada, USA): Spatiotemporal strain release in a strike-slip fault system: *Geosphere*, v. 15, no. 5, p. 1460–1478, <https://doi.org/10.1130/GES02088.1>.

Science Editor: David E. Fastovsky
Guest Associate Editor: Michael L. Williams

Received 17 November 2018
Revision received 22 March 2019
Accepted 5 June 2019

Published online 29 July 2019



This paper is published under the terms of the CC-BY-NC license.

© 2019 The Authors

Late Quaternary slip rates for faults of the central Walker Lane (Nevada, USA): Spatiotemporal strain release in a strike-slip fault system

Stephen J. Angster¹, Steven G. Wesnousky¹, Paula M. Figueiredo², Lewis A. Owen², and Sarah J. Hammer²

¹Center for Neotectonic Studies, University of Nevada, Reno, 1664 N. Virginia St., Reno, Nevada 89557, USA

²Department of Geology, University of Cincinnati, Cincinnati, Ohio 45221, USA

ABSTRACT

The Walker Lane is a broad shear zone that accommodates a significant portion of North American–Pacific plate relative transform motion through a complex of fault systems and block rotations. Analysis of digital elevation models, constructed from both lidar data and structure-from-motion modeling of unmanned aerial vehicle photography, in conjunction with ¹⁰Be and ³⁶Cl cosmogenic and optically stimulated luminescence dating define new Late Pleistocene to Holocene minimum strike-slip rates for the Benton Springs (1.5 ± 0.2 mm/yr), Petrified Springs (0.7 ± 0.1 mm/yr), Gumdrop Hills ($0.9^{+0.3}_{-0.2}$ mm/yr), and Indian Head (0.8 ± 0.1 mm/yr) faults of the central Walker Lane (Nevada, USA). Regional mapping of the fault traces within Quaternary deposits further show that the Indian Head and southern Benton Springs faults have had multiple Holocene ruptures, with inferred coseismic displacements of ~3 m, while absence of displaced Holocene deposits along the Agai Pah, Gumdrop Hills, northern Benton Springs, and Petrified Springs faults suggest they have not. Combining these observations and comparing them with geodetic estimates of deformation across the central Walker Lane, indicates that at least one-third of the ~8 mm/yr geodetic deformation budget has been focused across strike-slip faults, accommodated by only two of the five faults discussed here, during the Holocene, and possibly half from all the strike-slip faults during the Late Pleistocene. These results indicate secular variations of slip distribution and irregular recurrence intervals amongst the system of strike-slip faults. This makes the geodetic assessment of fault slip rates and return times of earthquakes on closely spaced strike-slip fault systems challenging. Moreover, it highlights the importance of understanding temporal variations of slip distribution within fault systems when comparing geologic and geodetic rates. Finally, the study provides examples of the importance and value in using observations of soil development in assessing the veracity of surface exposure ages determined with terrestrial cosmogenic nuclide analysis.

INTRODUCTION

Fault slip rates are fundamental to understanding earthquake recurrence of active faults, enabling probabilistic estimates of the timing and size of future earthquakes (e.g., Youngs and Coppersmith, 1985; Stein and Wysession, 2002;

McCalpin, 2009; Burbank and Anderson, 2012). New approaches in geodetic modeling have allowed slip rate estimates to be defined within models to yield contemporary slip rates (e.g., Sauber et al., 1994; Meade and Hager, 2005; Loveless and Meade, 2010; Hammond et al., 2011; Bormann et al., 2016), which may not be representative of longer-term strain release behavior. Variations in slip along individual faults (e.g., Kirby et al., 2006; Dolan et al., 2016; Frankel et al., 2007a, 2007b, 2011; Lee et al., 2009), seismic clustering (Rockwell et al., 2000; Kenner and Simons, 2005; Perouse and Wernicke, 2016), and slip partitioning between faults (Bennett et al., 2004; Pérouse and Wernicke, 2016) can promote temporal and spatial variations of strain release within fault systems. Here, we compare prior geodetic slip rate estimates with newly determined geologic slip rates, using additional geologic observations bearing on the relative recency of rupture, to understand the temporal and spatial behavior of late Quaternary slip across a series of subparallel strike-slip faults within the Walker Lane, a broad intraplate dextral shear zone (Fig. 1; Thatcher et al., 1999; Unruh et al., 2003; Faulds et al., 2005).

We focus our study in the central Walker Lane, where transtensional deformation occurs across a series of normal and strike-slip faults that lie between the eastern Sierra Nevada and western Basin and Range (Fig. 1; Unruh et al., 2003; Wesnousky, 2005a, 2005b; Wesnousky et al., 2012). There are five major subparallel active northwest striking strike-slip faults that define the northeastern boundary of the central Walker Lane (Nevada, USA): the Agai Pah, Gumdrop Hills, Indian Head, Benton Springs, and Petrified Springs faults (Fig. 1). At this latitude, geodesy indicates ~8 mm/yr of dextral shear across the ~140 km width of the central Walker Lane (Fig. 1; Hammond and Thatcher, 2004; Bormann et al., 2016). Reported long-term geologic slip rate estimates for the strike-slip faults are absent to limited (e.g., Wesnousky, 2005a), thus it remains unclear of the long-term total deformation accommodated by the strike-slip faults and how deformation occurs on temporal and spatial scales within this system of strike-slip faults.

We define new geologic rates of slip and compare with estimates of the relative recency and age of surface rupture for the central Walker Lane strike-slip faults based on regional-scale Quaternary fault mapping, using (1) digital elevation models (DEMs) constructed from airborne lidar and structure-from-motion (SfM) modeling of unmanned aerial vehicle photography, and (2) terrestrial cosmogenic nuclide (TCN) and optically stimulated luminescence (OSL) dating of displaced alluvial deposits. Probabilistic bounds on the rates of slip

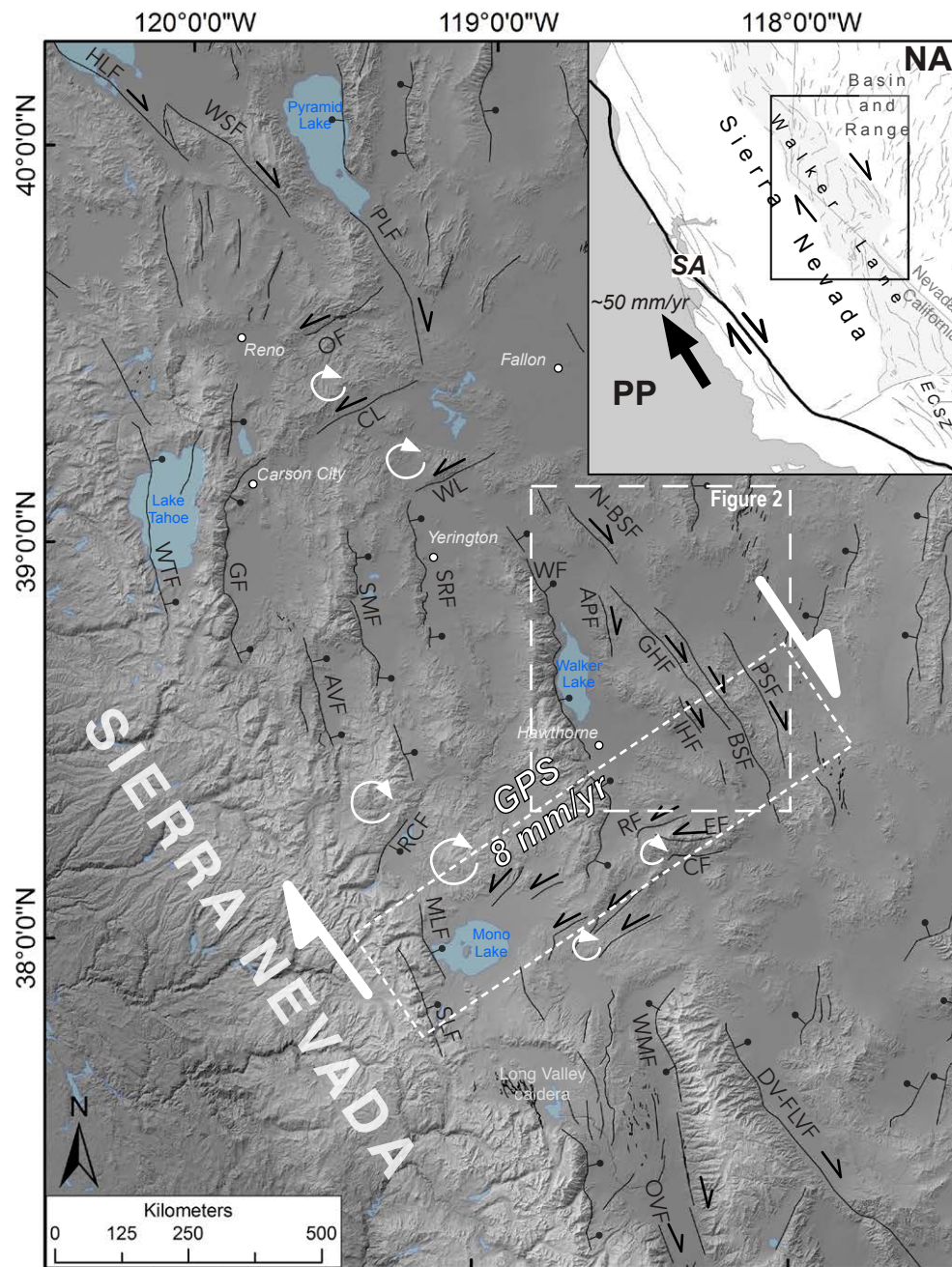


Figure 1. (Inset) Location of the Walker Lane (shaded), western United States. NA—North American plate; PP—Pacific plate; SA—San Andreas fault zone; ECSZ—eastern California shear zone. (Main) Shaded-relief image and fault map of the central portion of the Walker Lane. Quaternary-active fault traces (black lines) are modified from U.S. Geological Survey Quaternary Fault and Fold Database (<https://earthquake.usgs.gov/hazards/qfaults/>). Sense of motion on the faults is shown by black arrows on the strike-slip faults and half barbell on the down-dropped side of normal faults. White circular arrows show regions undergoing rotation (Cashman and Fontaine, 2000; Carlson et al., 2013). Solid white half arrows show relative motions, and white dashed box is representative of a geodetic strain rate transect across the central Walker Lane (Bormann et al., 2016). Studied faults: APF—Agai Pah fault; IHF—Indian Head fault; GHF—Gumdrop Hills fault; BSF—Benton Springs fault; N-BSF—northern Benton Springs fault; PSF—Petrified Springs fault. Other Quaternary-active faults of the Walker Lane: HLF—Honey Lake fault; WSF—Warm Springs fault; PLF—Pyramid Lake fault; OF—Olinghouse fault; CL—Carson lineament; WL—Wabuska lineament; WTF—West Tahoe fault; GF—Genoa fault; AVF—Antelope Valley fault; SMF—Smith Valley fault; SRF—Singatse Range fault; WF—Wassuk fault; RCF—Robinson Creek fault; MLF—Mono Lake fault; SLF—Silver Lake fault; RF—Rattlesnake fault; EF—Excelsior fault; CF—Coaldale fault; WMF—White Mountain fault; OVF—Owens Valley fault; DV-FLVF—Death Valley—Fish Lake Valley fault system.

are computed at targeted sites along four of the major strike-slip faults and provide the basis to compare geologic rates of deformation to those inferred geodetically in the central Walker Lane. The aim of the study is to better define the temporal and spatial pattern of slip across the strike-slip faults of the central Walker Lane and, as a result, also place a limit on the portion of slip that is being accommodated by faults to the west, where geologic evidence of long-term shear strain release remains elusive (e.g., Wesnousky et al., 2012; Bormann et al., 2016).

■ THE CENTRAL WALKER LANE

Geodesy shows the contemporary strain field of the Walker Lane to be generally right-lateral shear dominated, with the principle strain axis oriented to the northwest, while a secondary component of north-south extension is evident in the central and southern portions of the Walker Lane (e.g., Oldow et al., 2001; Kreemer et al., 2009; Bormann et al., 2016). Active transtensional deformation occurs in the central Walker Lane across a system of active north-west-trending right-lateral strike-slip faults (e.g., Stewart, 1988; Wesnousky, 2005a), north-south-oriented normal faults (Unruh et al., 2003; Wesnousky et al., 2012), and a conjugate set of northeast striking left-lateral faults (Rogers, 1975; Wesnousky, 2005a; Li et al., 2017) (Fig. 1). The pattern and structural style of faulting indicate long-term partitioning of the strain field, with east-west extension-dominated deformation on the normal faults to the west, and dextral shear deformation focused in the eastern portion of the central Walker Lane, across the strike-slip faults of this study (Fig. 1). Yet, neotectonic (Unruh et al., 2003; Wesnousky et al., 2012) and geodetic (Kreemer et al., 2009; Hammond et al., 2011; Bormann et al., 2016) studies find shear deformation to be more evenly distributed across the central Walker Lane, and have proposed several mechanisms of right-lateral shear strain release in the absence of strike-slip faulting, including: (1) block rotations of the normal fault-bounded blocks (Cashman and Fontaine, 2000; Wesnousky et al., 2012; Carlson et al., 2013); (2) oblique slip on the normal faults (Bormann et al., 2016); and (3) partitioned slip on strike-slip faults outboard of the range-bounding faults (Dong et al., 2014). Obtaining geologically based rates from geomorphic observations of dextral slip along the normal faults has remained challenging (e.g., Wesnousky et al., 2012; Bormann et al., 2016). We focus our attention to the east, where obtaining long-term horizontal slip rates appears to be more straightforward.

The strike-slip faults of the central Walker Lane strike subparallel to the contemporary northwest oriented shear strain field and record at least 34 km of cumulative right-lateral slip since the initiation of faulting (Ekren and Byers, 1984; Hardyman et al., 2000), which began as recently as 7 Ma to 10 Ma (Hardyman and Oldow, 1991). Prior geologic studies have provided qualitative Late Pleistocene slip rate estimates for only the Benton Springs (~1 mm/yr) and Petrified Springs (1.1–1.65 mm/yr) faults, relying on soil chronosequences and standard field techniques (Wesnousky, 2005a). Results from the geodetic block modeling of Bormann et al. (2016) predict a cumulative contemporary

slip rate of 0.91–3.15 mm/yr across the strike-slip faults of the central Walker Lane, providing a basis of comparison for longer-term rates derived in this study from geologic offsets.

■ QUATERNARY MAPPING

Methodology

Toward comparing the relative recency of late Quaternary surface rupture amongst the active strike-slip faults in the central Walker Lane, we compile prior geologic mapping of Quaternary formations and fault traces with new observations resulting from ~1:10,000-scale mapping performed in this study onto a regional map, shown in Figure 2, to highlight cross-cutting relationships of the central Walker Lane strike-slip faults with mapped Quaternary formations. Fault traces and Quaternary formation contacts are modified from the 1:48,000-scale geologic quadrangle maps of Carlson (2014), Ekren and Byers (1985a, 1985b, 1986a, 1986b), Greene et al. (1991), and Hardyman (1980), and Quaternary unit maps of Wesnousky (2005a), through analysis of modern ESRI World Imagery (https://services.arcgisonline.com/ArcGIS/rest/services/World_Imagery/MapServer) and Google Earth (<https://www.google.com/earth/>) satellite imagery, standard field mapping techniques, and analysis of airborne lidar data sets (1 m resolution) over the Benton Springs and Petrified Springs faults. The extent of lidar data coverage is shown in Figure 2, and the data are publicly available and described at OpenTopography (<https://www.opentopography.org>).

Alluvial fan formations are divided into three general units (Fig. 2; Qfo—Middle to Late Pleistocene; Qfi—Late Pleistocene; Qfy—Holocene), primarily based on variations in surficial characteristics (e.g., degree of incision, breadth and shape of interfluvies, and desert pavement development) following prior methods and general age delineations commonly applied to the region (Bull, 2008; Bell et al., 2004; Wesnousky, 2005a; Frankel et al., 2007a; Koehler and Wesnousky, 2011; Wesnousky and Caffee, 2011; Li et al., 2017). Descriptions of the mapped formations are provided in Supplemental Item A¹.

To better illustrate Holocene activity within detailed figures, we further subdivided the Holocene-age alluvial fan units (Qfy) into unit Qfy1, representative of active alluvium, and unit Qfy2, comprising older and higher alluvial surfaces. Fault traces are mapped within Quaternary deposits where fault scarps and lateral offsets are present. We also include the mapped traces of the faults through bedrock from the geological mapping to provide context of fault strike and location (Fig. 2).

Observations: Quaternary Expression and Recency of Surface Rupture

The Quaternary mapping along each of the central Walker Lane faults show the Indian Head and southern Benton Springs faults to exhibit fault scarps in Holocene alluvial fan deposits (unit Qfy; Fig. 2), while the surficial expressions

Appendix A: Regional Quaternary Mapping Unit Descriptions

Old alluvial deposits (Qfo) are deeply incised (>10 m) alluvial fan remnants that have well-developed drainage networks with smooth and well-rounded interfluvies. Qfo alluvial fan surfaces commonly have a desert pavement, varnished cobbles, and have well-developed soil profiles having a prominent Bt horizon, elevated rubification, and stage III⁺ carbonate development. Qfo surfaces are topographically higher than other alluvial fan surfaces and are inferred to be mid to late Pleistocene or older in age.

Intermediate age alluvial deposits (Qfi) exhibit lesser amounts of dissection, rest <10 m above modern stream grade, and have relatively broad, smooth, and flat surfaces. Soil profiles containing a B₁-horizon, some rubification, and stage II carbonate development are observed within Qfi deposits. The surfaces of Qfi fans are overprinted by lacustrine deposits (Ql) and shoreline scarp where they extend into the basin of and below the ~15.5 m highstand (~1314 m) of glacial Lake Lahontan (Benson and Thompson, 1987; Adams and Wesnousky, 1998, 1999). Based on comparison of carbonate development to other soils in the region (Adams and Wesnousky, 1999) and stratigraphic relationships with deposits of Lake Lahontan, we infer Qfi surfaces to be late Pleistocene in age.

The youngest alluvial fan deposits (Qfy) include the lowest alluvial fan surfaces and active channels. Qfy surfaces exhibit bar and swale topography, have minimal soil profile development, lacking a B₁-horizon, and buried lacustrine deposits and features associated with Lake Lahontan. Qfy deposits are considered to be Holocene in age. The basin fill (Qb) is comprised of distal active alluvial fan facies and active aeolian deposits of finer sediment.

The basin fill (Qb) is comprised of distal active alluvial fan facies and active aeolian deposits of finer sediment. Playa formations (Qp) are the remnant lake bottom of Lake Lahontan, now exposed, forming flat surfaces composed of fine silts and clay, and are considered Holocene in age.

¹Supplemental Material. Written descriptions of regionally mapped Quaternary units and sample collection, laboratory procedures, and data tables for geochronology. Please visit <https://doi.org/10.1130/GES02088.S1> or access the full-text article on www.gsapubs.org to view the Supplemental Material.

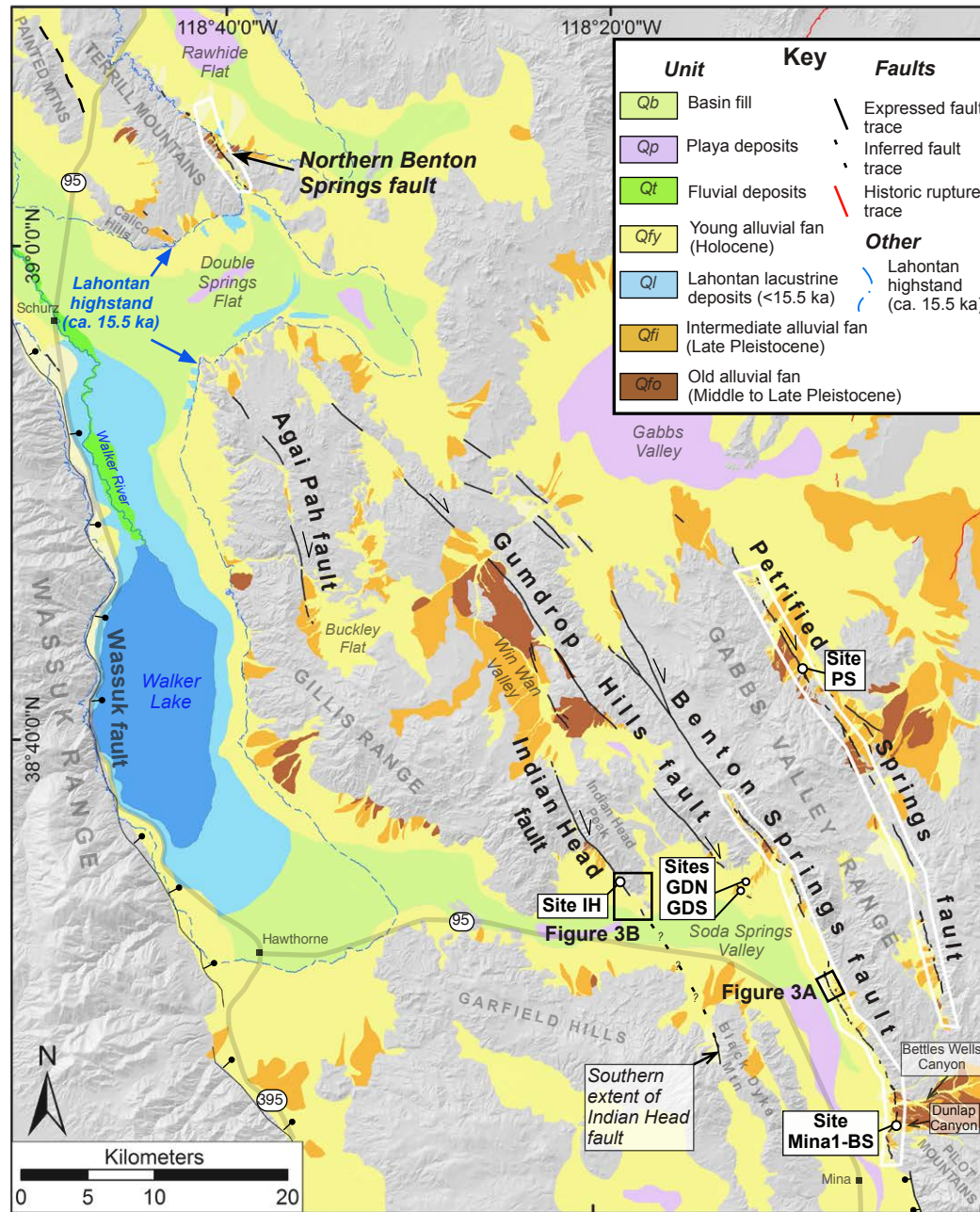


Figure 2. Quaternary unit and fault map of the study region. Quaternary units are shown in the key in order of relative age and are described in Supplemental Material A (text footnote 1). Mapped fault traces are limited to those displacing alluvial units, commonly forming scarps and lateral displacements. Areas of bedrock are gray, and fault traces from prior quadrangle mapping are included to provide reference to fault. Extent of the airborne lidar data sets are outlined in solid white lines.

of the Agai Pah, Gumdrop Hills, and Petrified Springs faults show scarps only within Middle to Late Pleistocene alluvial fan deposits (units Qfi and Qfo). The following describes the expression of Holocene faulting along the Benton Springs and Indian Head faults.

The Holocene fault trace of the Benton Springs fault extends discontinuously for ~40 km, from the southern end to the northern end of Soda Springs Valley (Fig. 2). The Holocene expression is most pronounced north of Dunlap Canyon (Fig. 2) where the fault diverts from the Gabbs Valley Range front and forms subtle west-facing discontinuous fault scarps within older Holocene alluvial fans in Soda Springs Valley (Fig. 3A). An incised drainage channel is right-laterally offset by ~3 m (Fig. 3A) within the Holocene alluvial fans. Prior trenching farther to the south in Dunlap Canyon (Fig. 2) shows evidence for an 800 ¹⁴C yr B.P. surface-rupturing earthquake (Wesnousky, 2005a). The observed Holocene fault trace and associated lateral offset of ~3 m, located <15 km northwest of the trench, are likely the result of the earthquake event observed in the trench.

Faulting of Holocene deposits along the trace of the Benton Springs fault is limited to the southern segment of the fault located within Soda Springs Valley, and not recognized immediately northward where the fault cuts through the bedrock of the Gabbs Valley Range (Fig. 2). Farther north, expression of the same fault is buried by unit Qfy alluvial fans and limited to Middle to Late Pleistocene alluvial fans (units Qfi and Qfo; Fig. 2). Analysis of the northernmost lidar data set along the eastern flank of the Terrill Mountains (Fig. 2) shows the fault trace to be concealed by post-Lahontan highstand (15.5 ka; Adams and Wesnousky, 1999) alluvial fan deposits (Fig. 2). These observations indicate that the northern portion of the Benton Springs fault, beyond where the fault cuts through the Gabbs Valley Range (Fig. 2), has probably not ruptured during the Holocene, and the most recent rupture(s) was limited to the southern segment within Soda Springs Valley.

Holocene rupture on the Indian Head fault is displayed at the southern end of the Indian Head Peak ridge within Soda Springs Valley (Fig. 3B) as <0.5-m-high scarps manifested within unit Qfy2 alluvial fans, which have surfaces that are darker in color than, and sit slightly above, the active alluvium (Fig. 3B). An 8 m right-lateral offset of an alluvial fan-terrace riser is recorded by these deposits (Fig. 3B). The Holocene trace of the Indian Head fault is also observed north of the Gillis Range within Win Wan Valley (Fig. 2), showing similar characteristics of short discontinuous scarps within older Holocene alluvial fan surfaces, and after a short distance, dies out within the Holocene alluvial fan deposits in Win Wan Valley (Fig. 2).

South of U.S. Highway 95 and along strike of the Indian Head fault, an active fault trace trends along the western flank of the Black Dyke Mountain (Fig. 2). The fault trace also forms subtle (<0.5 m high) west-facing fault scarps within older Holocene alluvial fans. The expression of this southern fault strand is similar to that of the strand along the Indian Head Peak ridge. No fault scarps are observed within the younger Holocene basin-fill deposits and are likely concealed by the active basin-fill deposits in Soda Springs Valley between Black Dyke Mountain and the Indian Head Peak ridge (Fig. 2). Due to the similarity of expression and linearity of the two traces, we interpret

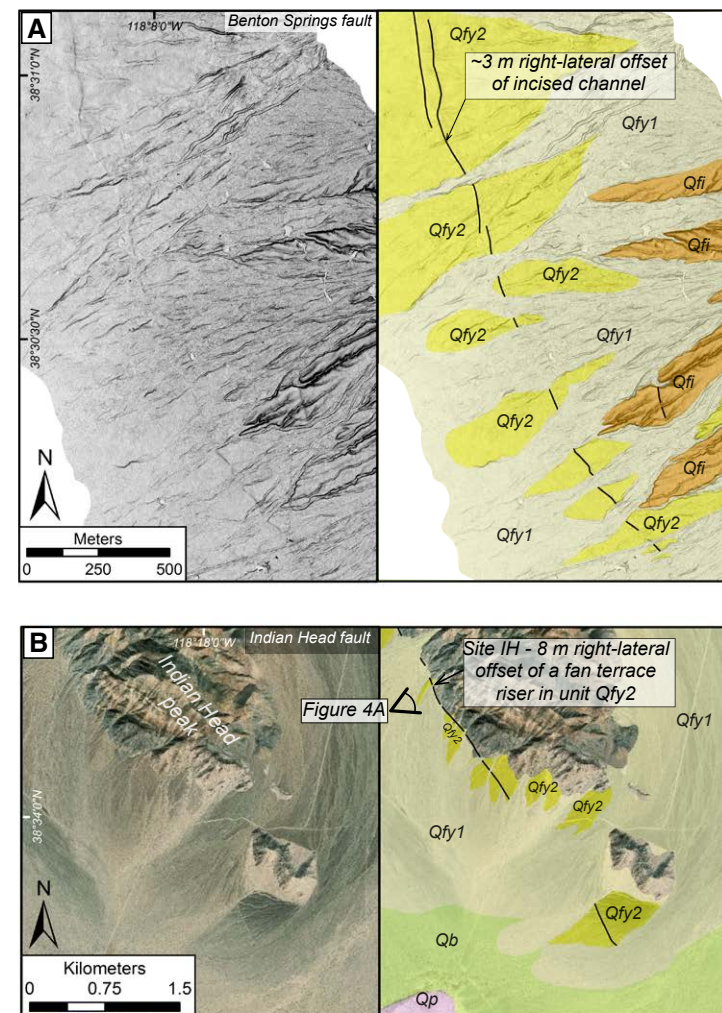


Figure 3. Holocene expression of faulting along the Benton Springs fault (A) and Indian Head fault (B). Locations of figures are shown in Figure 2. (A) Uninterpreted slope-shade image from lidar data (left) and interpreted fault and Quaternary unit map (right) of the Benton Springs fault area. (B) Uninterpreted ESRI World Imagery image (left) and fault and Quaternary unit map (right) of the Indian Head fault area. Geologic unit and fault trace explanations are provided in Figure 2 and follow descriptions provided in Supplemental Material A (footnote 1). Unit Qfy2 denotes older Holocene alluvial fan elements, and unit Qfy1 is the active alluvium.

the Black Dyke Mountain fault strand to be the southern continuation of the Indian Head fault, and the Holocene trace to be concealed by the active distal fan and aeolian deposits within Soda Springs Valley. This extends the total fault length to ~40 km (Fig. 2).

In summary, the above observations indicate that both the Indian Head and southern Benton Springs faults have ruptured at least once during the Holocene, while the absence of displaced Holocene deposits along the Agai Pah, Gumdrop Hills, northern Benton Springs, and Petrified Springs faults indicate that they have not. Furthermore, the spatial distribution of Holocene rupture within central Walker Lane strike-slip fault system is observed to have been more focused at the southern end within Soda Springs Valley (Fig. 2).

■ SLIP RATE SITE DESCRIPTIONS AND HORIZONTAL DISPLACEMENTS

Geological slip rates are determined at selected locations along the faults: (1) that provide a clear measurable geomorphic offset; (2) where the age of offset deposits may be assessed with quantitative Quaternary dating methods; and (3) where the offsets are considered to be the product of at least two or more earthquakes. The site locations include: site IH on the Indian Head fault, sites GDN and GDS on the Gumdrop Hills fault, site Mina1-BS on the Benton Springs fault, and site PS on the Petrified Springs fault (Fig. 2). No measurable lateral offset along the Agai Pah fault is evident from the regional mapping, thus no rate is obtained for this fault. The reported measures of horizontal offset are made from field observations aided by high-resolution DEMs constructed from either the lidar data sets or SfM modeling of drone photography, analyzed with Agisoft Photoscan software, following the approach of Angster et al. (2016). To formalize the offset measurements and evaluate the associated uncertainty, we utilize the Matlab script *LaDiCaoz_v2.1* (Zielke et al., 2012; Had-don et al., 2016), which calculates an optimal offset based on cross-correlation of topographic profiles extracted from high-resolution DEMs drawn across geomorphic features on either side of the fault.

Site IH

The Indian Head fault displaces a Holocene unit Qfy alluvial fan sourced from a proximal small steep canyon near the southern end of the Indian Head Peak ridge (Figs. 2, 3A, and 4A). The alluvial fan surface sits ~1.5 m above the active drainage and is characterized by muted bar-and-swale topography constructed by angular metasedimentary gravel and scattered small angular boulders. The fault forms an ~1-m-high southwest-facing scarp near the bedrock contact and right-laterally offsets the southern alluvial fan-terrace riser, which is present on both sides of the fault (Fig. 4B). The riser crest and base are offset 7.6 and 8.3 m, respectively, yielding a best estimate of the offset equal to 8 ± 0.4 m (Figs. 4B and 4C). The relative consistency of offset between the

measured riser and base suggest that offset occurred after deposition and full abandonment of the alluvial fan surface.

Sites GDN and GDS

The Quaternary trace at the southern end of the Gumdrop Hills fault splays into two subparallel fault traces, forming a graben within the distal portion of a unit Qfi alluvial fan in Soda Springs Valley that is sourced from a large canyon to the northeast (Fig. 2 and 5A). On the northern fault strand (site GDN; Fig. 5A), the fault exhibits an ~3-m-high southeast-facing fault scarp within the unit Qfi alluvial fan and right-laterally deflects an incised drainage channel and offsets the southeastern alluvial fan-terrace riser of the unit Qfi alluvial fan (Fig. 5B). The crest and base of the riser record 11 and 14.2 m (12.6 ± 1.6 m) of right-lateral displacement, respectively (Figs. 5B and 5D). The southern fault strand (site GDS; Fig. 5A) forms an ~0.5 m northeast-facing scarp within the same unit Qfi alluvial fan and right-laterally displaces the northwestern alluvial fan-terrace riser base and crest 4.2 and 5.1 m (4.6 ± 0.5 m), respectively (Figs. 5C and 5E). The measured offsets accrued post-deposition of the alluvial fan, and sum to a cumulative average displacement of 17.1 ± 2.5 m across the two fault strands.

Site Mina 1-BS

Near the southern end of the Benton Springs fault, the fault crosses in front of the Dunlap Canyon outlet at Site Mina 1-BS and forms a linear west-facing scarp within a series alluvial fans that emanated from the large canyon (Figs. 2 and 6A). On the northern side of the active drainage channel, the fault forms an ~2-m-high scarp and right-laterally displaces the southern riser of a unit Qfi alluvial fan (Fig. 6B). Reconstruction of the alluvial fan riser crest, slope, and base provides relatively consistent offset measurements of 36, 34.2, and 33 m, respectively (Fig. 6C). The three offsets average 34.5 ± 1.5 m and occurred sometime after abandonment of the alluvial fan.

Site PS

Site PS is located along the northern end of the Petrified Springs fault (Fig. 2), where the fault follows a very linear trace, defined by a predominantly north-east-facing scarp where it displaces distal portions of unit Qfi and Qfo alluvial fans (Fig. 7A). A beheaded channel, incised into a unit Qfi alluvial fan, is preserved on the east side of the fault trace and lies below a large fault scarp that preserves a high unit Qfo alluvial fan terrace surface (Figs. 7A and 7B). Reconstruction of the base and crest of the southern channel margin of the beheaded channel to the northern prow end of the bedrock ridge on the south side of the active channel yields an offset measurement of 92.5 ± 0.5 m (Fig. 7C). The offset accrued after the incision of the beheaded channel into the unit Qfi alluvial fan.

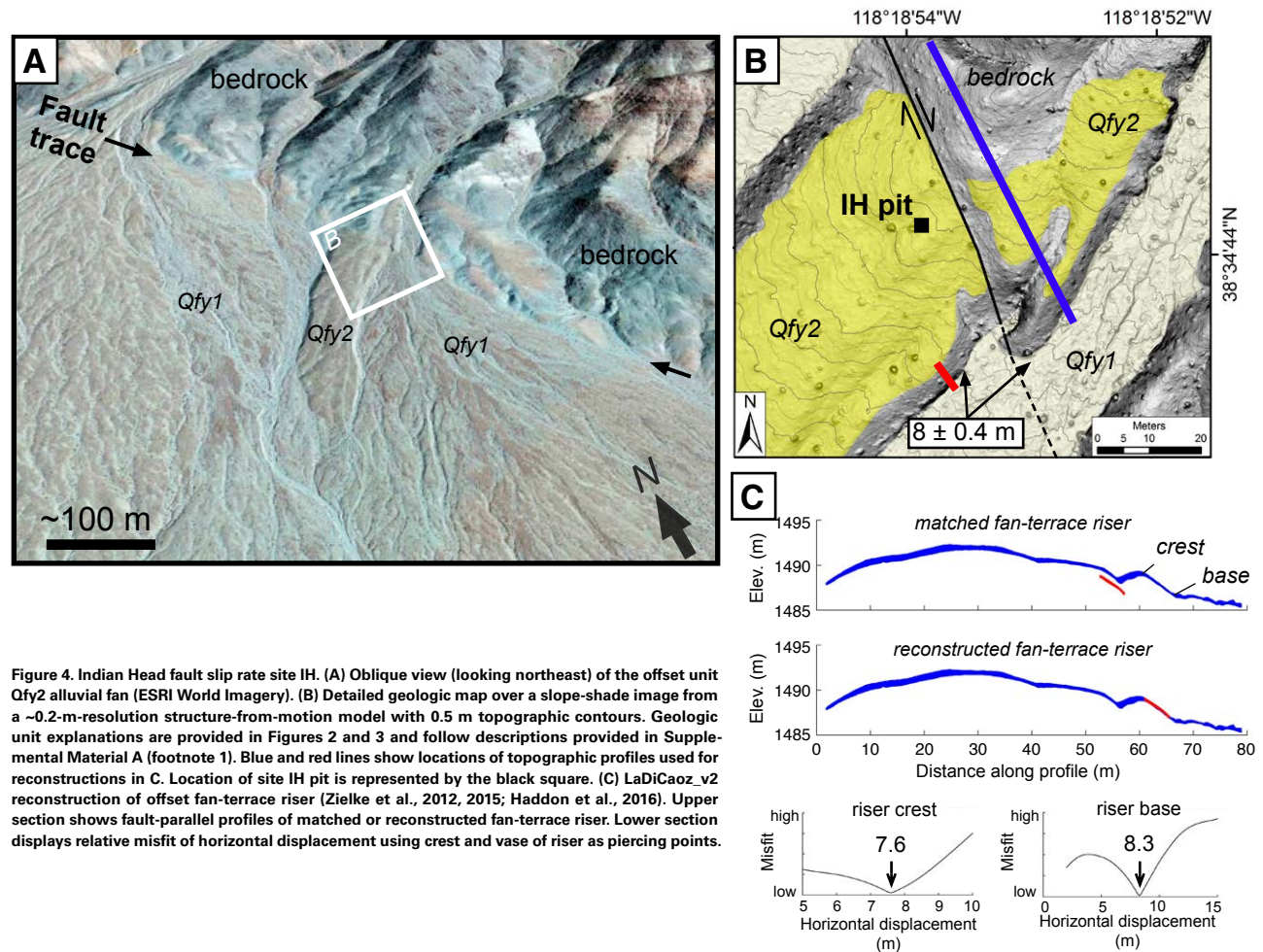


Figure 4. Indian Head fault slip rate site IH. (A) Oblique view (looking northeast) of the offset unit Qfy2 alluvial fan (ESRI World Imagery). (B) Detailed geologic map over a slope-shade image from a ~0.2-m-resolution structure-from-motion model with 0.5 m topographic contours. Geologic unit explanations are provided in Figures 2 and 3 and follow descriptions provided in Supplemental Material A (footnote 1). Blue and red lines show locations of topographic profiles used for reconstructions in C. Location of site IH pit is represented by the black square. (C) LaDiCaoz_v2 reconstruction of offset fan-terrace riser (Zielke et al., 2012, 2015; Haddon et al., 2016). Upper section shows fault-parallel profiles of matched or reconstructed fan-terrace riser. Lower section displays relative misfit of horizontal displacement using crest and base of riser as piercing points.

■ GEOCHRONOLOGY

Measurements of in situ concentrations of TCNs ^{10}Be and ^{36}Cl are used as a primary method to place numerical age limits on the timing of alluvial fan formation at each slip-rate study site. TCNs accumulate at a relatively well-known rate resulting from the interaction of cosmic rays with certain minerals at Earth's surface, which systematically decay with depth, allowing for the duration of surface exposure to be quantified (Gosse and Phillips, 2001). We use TCN depth profiles to mitigate the uncertainty of inheritance (e.g., Gosse and Phillips, 2001) and surface samples where possible. The details of sample

collection, processing methods, and age modeling are provided in Supplemental Material B (footnote 1), and the associated Tables SB1 and SB2 provide a summary of sample data, measured ^{10}Be and ^{36}Cl concentrations from the Purdue Rare Isotope Measurement (PRIME) Laboratory (West Lafayette, Indiana, USA), and parameters used for age modeling. Results of the ^{10}Be and ^{36}Cl profile age modeling are provided in Tables 1 and 2, respectively. At one location, OSL analysis of a buried sand lens within an alluvial fan deposit is used to further constrain the age of a displaced alluvial fan surface. Details of the OSL sample collection and laboratory processing methods performed at the University of Cincinnati (Ohio, USA) are also provided in Supplemental Material B. In

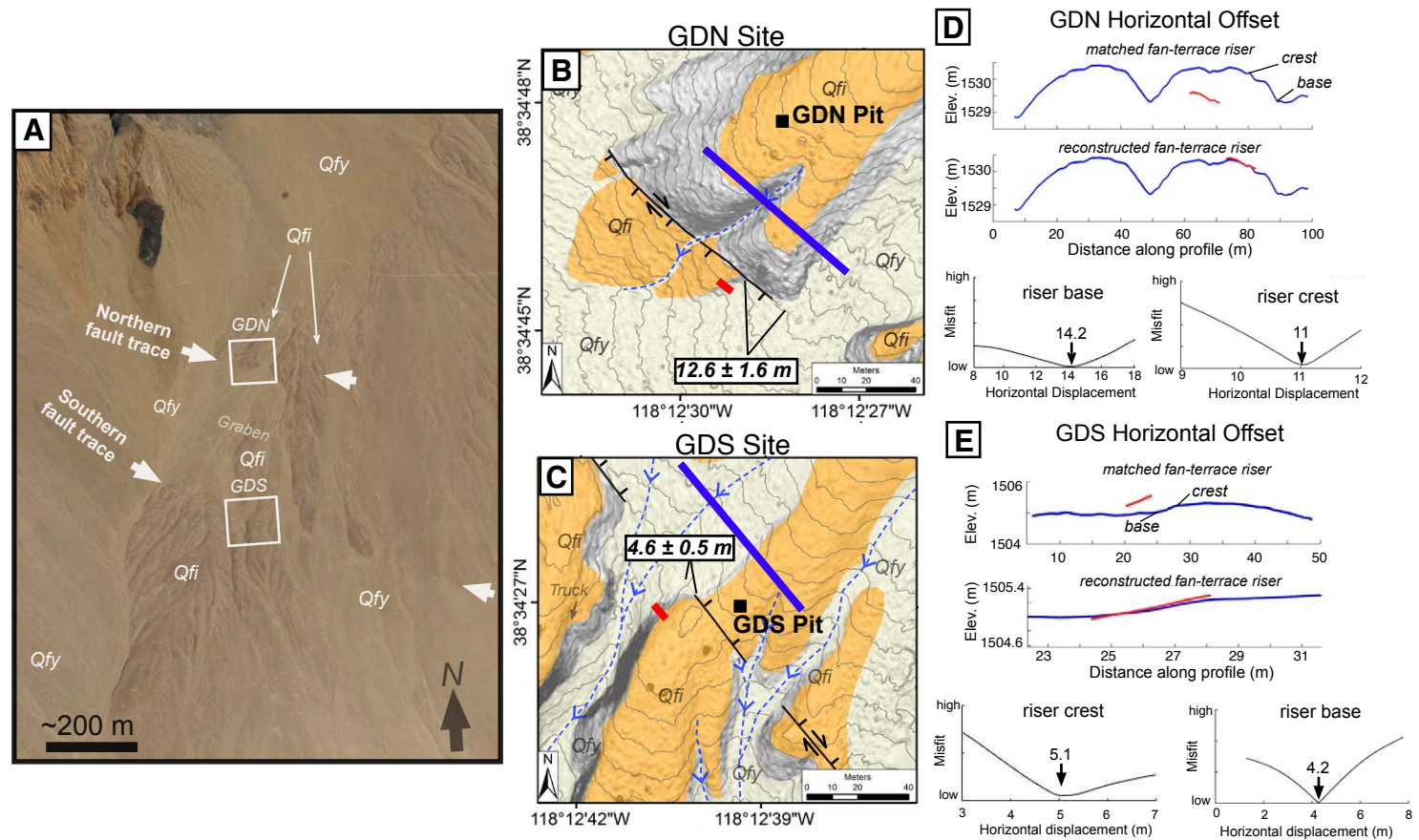


Figure 5. Gumdrops Hills fault slip rate sites GDN and GDS. (A) Oblique view (looking northeast) of offset distal unit *Q_{fi}* alluvial fan unit (ESRI World Imagery). White arrows point toward Quaternary trace of fault. (B and C) Detailed geologic maps over structure-from-motion slope-shade images and 0.5 m topographic contours showing measured offsets. Geologic unit explanations are provided in Figures 2 and 3 and follow descriptions provided in Supplemental Material A (footnote 1). Locations of site GDN and GDS ¹⁰Be and ³⁶Cl cosmogenic pits are represented by black squares. Blue and red lines correspond to topographic profiles used for reconstructions shown in D and E. (D and E) LaDiCaoz_v2 reconstruction of offset fan-terrace riser (Zielke et al., 2012, 2015; Haddon et al., 2016). Upper section shows fault-parallel profiles of matched or reconstructed fan-terrace riser. Lower section displays relative misfit of horizontal displacement using crest and base of riser as piercing points.

addition to the numerical dating methods, soil profile descriptions of each pit exposure are recorded following the techniques and terminology described by Birkeland (1984) and Soil Survey Division Staff (1993). Characteristics such as soil thickness, clay content, carbonate stage, and development of B-horizons have been observed to increase as a function of time (e.g., Bachman and Machette, 1977; Machette, 1985; Birkeland, 1984; Harden et al., 1991), and are used to assess relative ages of the offset alluvial surfaces and compared with the results from the TCN and OSL analyses. Soil profile characteristics of each pit are provided in Table SB3 (footnote 1).

Site IH Pit

The location of the pit excavated on the surface of the displaced unit *Q_{fy2}* alluvial fan surface at site IH along the Indian Head fault is shown in Figure 4B and sits ~2 m above the active alluvium. The displaced surface is characterized by muted bar-and-swale topography and has poorly developed desert pavement within the interfluvies. The pit was dug into an interfluvial surface and exposed a poorly sorted unconsolidated massive conglomerate composed of angular pebbles and cobbles, capped by faint soil characterized by a 7-cm-thick silt-rich Av-horizon

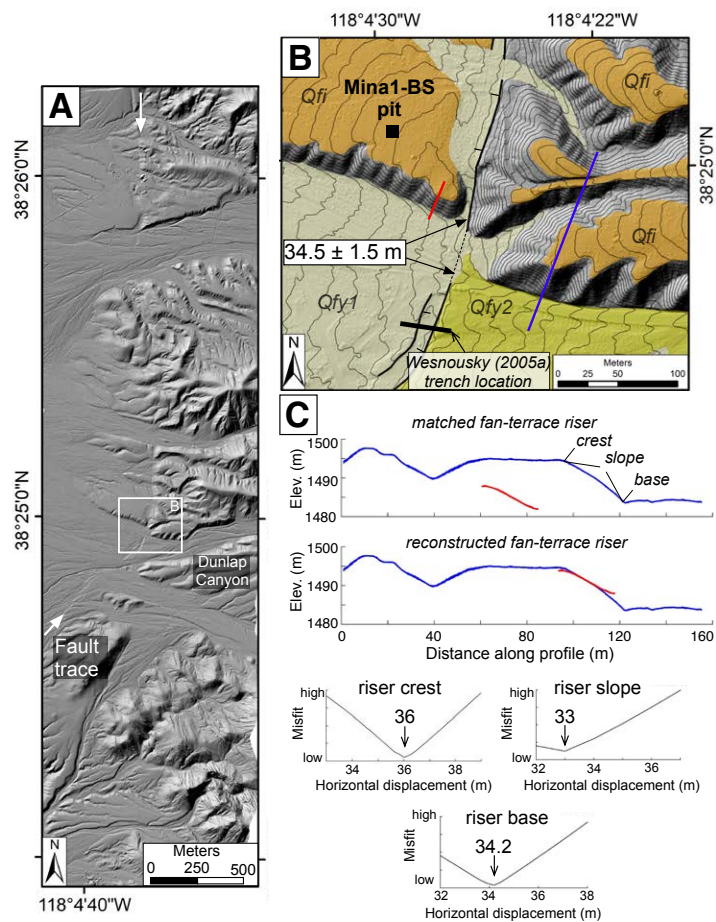


Figure 6. Benton Springs fault slip rate site Mina1-BS. (A) Shaded-relief image of lidar data over the southern portion of the Benton Springs fault. (B) Detailed geologic map within 0.5 m topographic contour intervals. Geologic unit explanations are provided in Figures 2 and 3 and follow descriptions provided in Supplemental Material A (footnote 1). Location of site Mina1-BS pit is shown by the black square. Blue and red lines correspond to topographic profiles used for reconstructions shown in C. (C) LaDiCaoz_v2 reconstruction of offset fan-terrace riser (Zielke et al., 2012, 2015; Haddon et al., 2016). Upper section shows fault-parallel profiles of matched or reconstructed fan-terrace riser. Lower section displays relative misfit of horizontal displacement using crest and base of riser as piercing points.

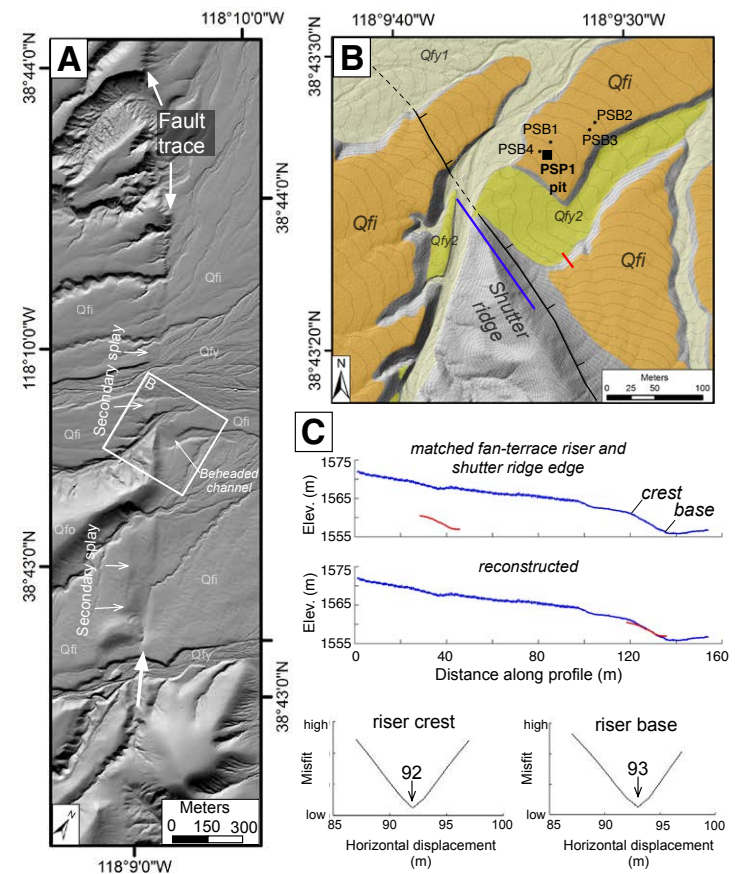


Figure 7. Petrified Springs fault slip rate site PS. (A) Shaded-relief image of lidar data along the northern portion of the Petrified Springs fault. (B) Detailed geologic map with 0.5 m topographic contour intervals. Geologic unit explanations are provided in Figures 2 and 3 and follow descriptions provided in Supplemental Material A (footnote 1). Location of pit PSP1 is shown by a black square, and boulder samples PSB1–PSB4 are shown by black dots. Blue and red lines correspond to topographic profiles used for reconstructions shown in C. (C) LaDiCaoz_v2 reconstruction of offset fan-terrace riser (Zielke et al., 2012, 2015; Haddon et al., 2016). Upper section shows fault-parallel profiles of matched or reconstructed fan-terrace riser. Lower section displays relative misfit of horizontal displacement using crest and base of riser as piercing points.

TABLE 1. BAYESIAN MOST PROBABLE ¹⁰Be PROFILE SURFACE AGES

¹⁰ Be depth profile	Surface age (ka)	Inheritance (10 ⁴ atoms g ⁻¹)	Erosion rate (cm ka ⁻¹)
Mina1-BS	21.7 ^{+10.8} / _{-7.1}	40.38 ^{+2.6} / _{-2.84}	0.84 ^{+0.14} / _{-0.82}
GDS	73.8 ^{+39.6} / _{-18.6}	30.33 ^{+4.81} / _{-3.59}	0.23 ^{+0.03} / ₋₁
IH	10.4 ^{+37.1} / _{-0.3}	38.35 ^{+2.17} / _{-3.18}	0.61 ^{+0.36} / _{-0.41}

Note: ¹⁰Be profile age results from Hidy et al. (2010) calculator. Input parameters for calculations are provided in Table SB1 (see text footnote 1).

TABLE 2. BAYESIAN MOST PROBABLE ³⁶Cl PROFILE SURFACE AGES

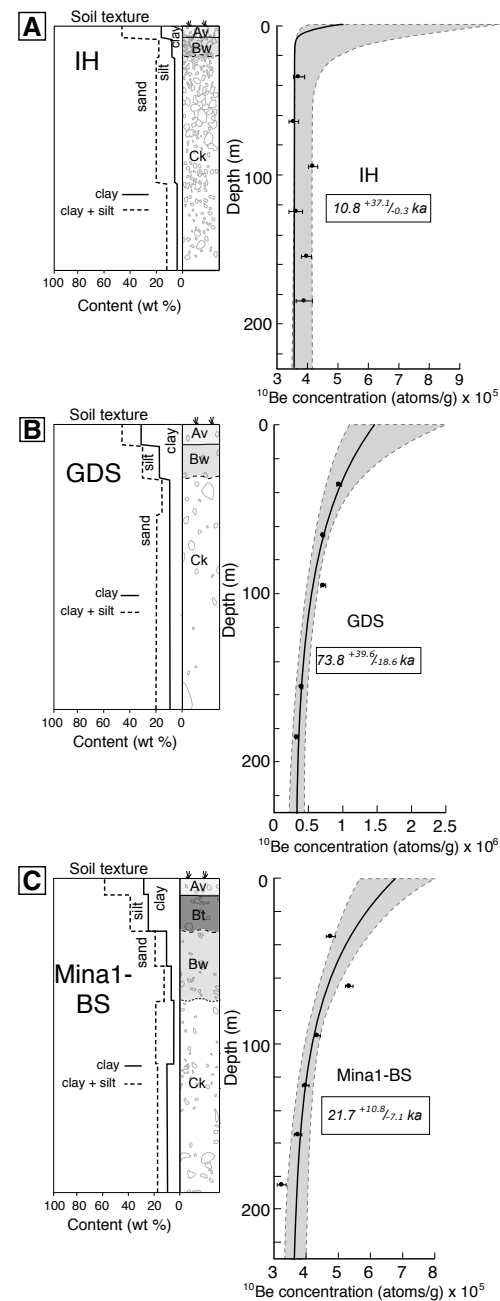
³⁶ Cl depth profile	Surface age (ka)	Inheritance (10 ⁴ ka)	Erosion rate (g/cm ² /k.y.)
GDS	61.4 ± 1.2	31.3	0–0.06
GDN	70.2 ± 5.7	22.0	0–0.06
PSP1	153.5 ± 11.2	25.4	0–0.43

Note: ³⁶Cl profile age results from CRONUScalc (Marrero et al., 2016). Input parameters for calculations are provided in Table SB2 (see text footnote 1).

underlain by an 11-cm-thick Bw-horizon and stage I carbonate development (Machette, 1985) (Fig. 8A; Table SB3 [footnote 1]). The weak soil development suggests this surface to be no older than Holocene in age. The ¹⁰Be concentrations of six samples, collected within the pit at 30 cm intervals, are similar throughout the entire depth profile (Fig. 8A), showing no systematic decrease with depth. Modeling of the concentrations using the Hidy et al. (2010) depth profile Monte Carlo age modeler provides a surface age of 10.4 ^{+37.1}/_{-0.3} ka (Table 1).

There are several observations that lead us to disregarding the upper age bound of the ¹⁰Be profile age result. First, the lack of a systematic decrease of ¹⁰Be concentration with depth observed in the site IH cosmogenic profile (Fig. 8A) is generally symptomatic of a younger deposit (Owen et al., 2011), where the inherited TCN signal is likely exceeding the concentrations of ¹⁰Be produced in situ. Second, the large positive uncertainty (+37 ka) might not reflect a natural condition but rather be a result of the software modeling settings selected for the best fit, which might have forced an expected increase in

Figure 8. Pit characteristics and ¹⁰Be concentrations for pits at sites IH (Indian Head fault) (A), GDS (Gumdrop Hills fault) (B), and Mina1-BS (Benton Springs fault) (C). Left panel shows generalized stratigraphic column and soil texture plot (solid line indicates clay content, and dashed line indicates clay + sand content). Samples of each soil horizon were textured at A&L Great Lakes Laboratory (Fort Wayne, Indiana) for particle-size analysis. Detailed descriptions of each soil are provided in Table SA1 (footnote 1). Right panel shows ¹⁰Be concentrations versus depth profiles. Solid black circles show sample concentrations and associated uncertainty of the total measured error (Table B1). Grey areas represent the span of 100,000 profile simulations using the Hidy et al. (2010) calculator and black lines show best-fit output. Preferred age provided in the white box. Locations of each pit are shown in Figures 4B, 5C, and 6B.



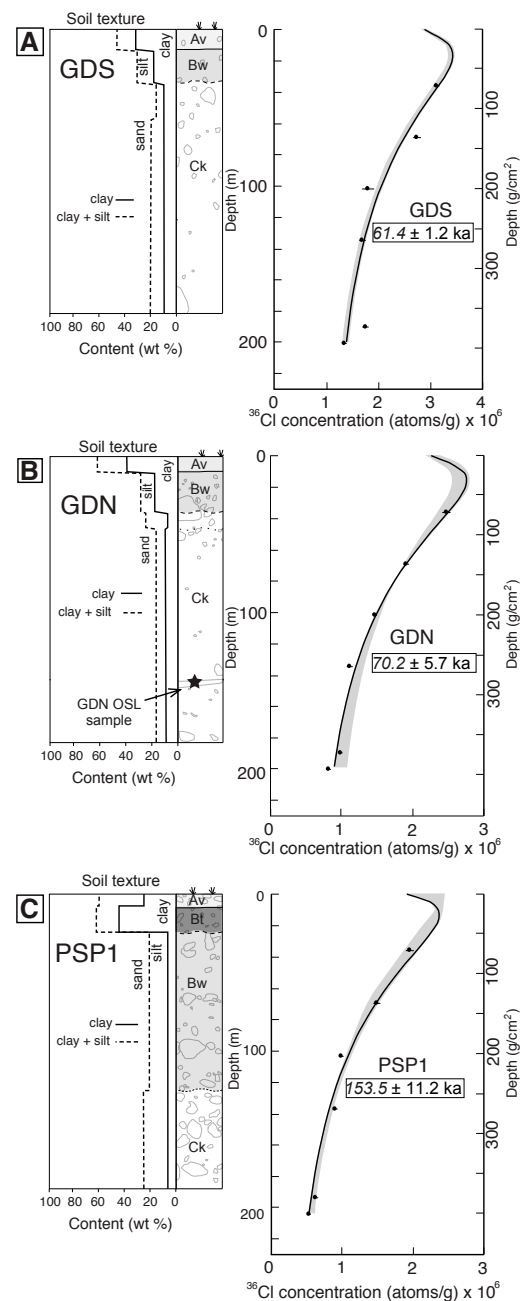
concentration near the surface (<30 cm) (Fig. 8A). The increase expressed by a rollover of the depth profile near the surface is not reflected by the sample concentrations and is likely not real. Finally, the weak soil and the geomorphic expression of the alluvial fan, exhibited by bar-and-swale topography and little desert pavement development, corroborate a Holocene surface. Together, these observations indicate that the lower end of the ^{10}Be age (10.8–10.5 ka) more likely represents the depositional age of the unit Qfy2 alluvial fan (Fig. 4B).

Site GDN and GDS Pits

Pits were dug into the dissected unit Qfi alluvial fan at slip-rate sites GDN and GDS along the Gumdrop Hills fault (Figs. 5B and 5C). The surfaces of the unit Qfi alluvial fan at both sites are correlative and display relatively smooth gently dipping surfaces that have a moderately developed desert pavement and are sparsely vegetated. Both pits exposed similar lithologies of poorly sorted angular to subangular massive pebble-cobble conglomerate (Figs. 9A and 9B). The soil in the site GDS pit is characterized by a 19-cm-thick sandy clay loam Av-horizon underlain by an ~25-cm-thick sandy loam Bw-horizon (Fig. 8B) with stage I carbonate development (Machette, 1985) extending ~1.5 m below the surface (Table SB3 [footnote 1]). The soil observed in the site GDN pit is found to be similar, characterized by a 10-cm-thick silty loam Av-horizon underlain by an ~15-cm-thick sandy loam Bw-horizon (Fig. 9B), and also having stage I carbonate development extending through the entire profile (Table SB3). The thicker Bw-horizons observed in these two pits show that these soils are more developed than the soil observed in the site IH pit, and are comparable to the regional soils associated with the 15.5 ka Lahontan highstand and calibrated with geochronology data (e.g., Adams and Wesnousky, 1999; Benson, 1978; Reheis et al., 1989; McFadden et al., 1998). On this basis, we interpret this surface to be ca. 15.5 ka in age.

The ^{10}Be and ^{36}Cl concentrations of six profile samples collected from the site GDS pit are plotted in Figures 8B and 9A, respectively. The ^{10}Be concentrations of the site GDS pit show a systematic decrease with depth (Fig. 8B), despite the sample from 100 cm depth showing a slight variance from the predicted modeling of Hidy et al. (2010). The best-fit profile provides an age of $73.8^{+39.6}_{-18.6}$ ka (Table 1). The ^{36}Cl concentrations for the site GDS pit also display a general decrease of concentration with depth, however there is more variance of the concentrations from the predicted modeling (Fig. 9A),

Figure 9. Pit characteristics and cosmogenic ^{36}Cl concentration modeling at sites GDS (Gumdrop Hills fault) (A), GDN (Gumdrop Hills fault) (B), and PS (Petrified Springs fault) (C). Left panel shows soil texture plot (solid line indicates clay content, and dashed line indicates clay + sand content) and soil horizons on simplified sedimentary column. Right panel shows ^{36}Cl concentrations versus depth profile plots. Right vertical axes provide depth in mass-length units assuming a density of 2.2. Solid black circles show sample concentrations and associated uncertainty of the total measured error (Table B2 [text footnote 1]). Grey areas represent the span of 100,000 Monte Carlo profile simulations using CRONUScal (Marrero et al., 2016) and black lines show best-fit output. Preferred age provided in the white box. Locations of each site are shown in Figures 5B, 5C, and 7B.



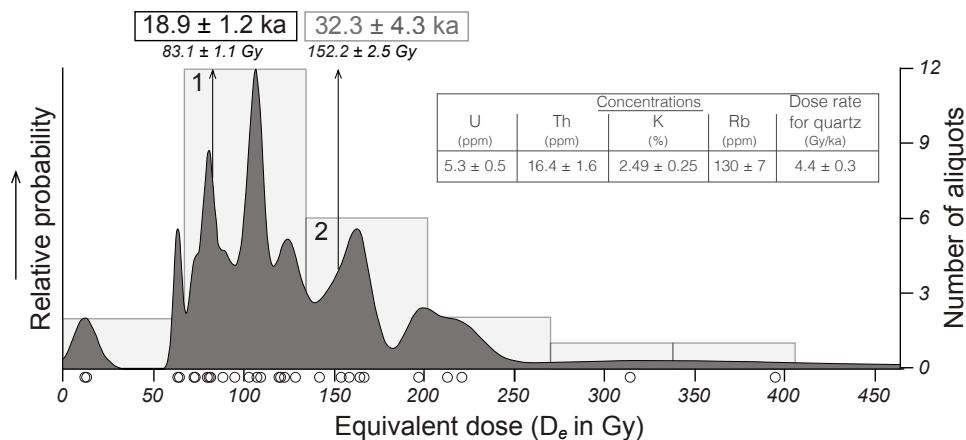


Figure 10. Relative probability and histogram plot of 24 aliquot measurements (hollow circles) showing equivalent dose (D_e) distribution of the optically stimulated luminescence sample collected in the site GDN pit (Gumdrop Hills fault; Figs. 5A and 9B). Table shows measured concentrations of U, Th, K, and Rb for the dose rate calculation. We assume a 10% error in the calculation. Two statistically significant peaks at $\sim 761 D_e$ (peak 1) and $\sim 1395 D_e$ (peak 2) are identified using the RadialPlotter application (Vermeesch, 2009), providing ages of 18.9 ± 1.2 ka and 32.3 ± 4.3 ka for peaks 1 and 2, respectively, using a dose rate value of 4.4 ± 0.27 Gy/k.y. We interpret peak 1 (18.9 ± 1.2 ka) to most likely represent the last exposure event, and peak 2 to be representative of partially bleached grains.

which yields a preferred age of 61.4 ± 1.2 ka (Table 2). The ^{36}Cl concentrations for the site GDN pit profile show more agreement with the modeling (Fig. 9B) and provide an age of 70.2 ± 5.7 ka (Table 2), providing an age range of 60–71 ka for this unit Qfi alluvial fan surface based on TCN ^{36}Cl . We were unable to perform ^{10}Be analysis within the site GDN pit due to low quartz yield for some fractions of the depth profile, and ^{10}Be results from the GDS depth profile provide an age range of 113–55 ka. Although ^{36}Cl age calculations fall within ^{10}Be age range, both TCN analyses are much older than the interpreted ca. 15.5 ka younger age of the soils observed in both pits. Despite the lack of quartz, we successfully obtained an OSL sample from a lens of fine- to medium-grained sand at ~ 1.5 m below the surface within the site GDN pit (Fig. 9B). Details of sample collection and processing are provided in Supplemental Material B (footnote 1). The OSL sample yields an age of 18.9 ± 1.2 ka (Fig. 10).

The age results for the unit Qfi surface at sites GDN and GDS determined from the TCNs, OSL analysis, and interpreted age of the soil are compared in Figure 11. The TCN ages span 113.4 to 55.2 ka and do not overlap with the much younger age of the OSL sample (18.9 ± 1.2 ka) (Fig. 11). There are several observations that lead us to interpret that the younger OSL age of the deposit is more representative of the age of the surface than the age range indicated by the TCN analysis. First, a soil developed on a surface of 60–80 ka or slightly older as suggested by the cosmogenic analysis would be expected to display a significant Bt-horizon and a more advanced carbonate development stage (e.g., Harden et al., 1991; Machette, 1985), which are not observed. Second, the weak soil development observed within the two pits (Fig. 11) is consistent with the age result of the OSL sample, which is representative of the deposition time of the sand lens. The sand lens lies ~ 1.5 m below the surface, thus it is older than the alluvial fan surface, and the OSL age provides a maximum age for the fan surface. On these bases, we interpret the OSL age (18.9 ± 1.2 ka) to represent the maximum age of the unit Qfi alluvial fan surface at sites GDN and GDS.

Site Mina1-BS Pit

The site Mina1-BS pit is located on the displaced unit Qfi alluvial fan surface along the Benton Springs fault (Fig. 6B). The unit Qfi fan surface at this site sits ~ 5 m above the active channel and is mantled by a well-developed desert pavement that is sparsely vegetated. The pit exposes a poorly sorted, massive, subrounded pebble conglomerate with a moderately developed soil established within the upper ~ 90 cm of the surface, characterized by an ~ 20 -cm-thick rubified Bt-horizon (Fig. 8C) and stage II carbonate development (Machette,

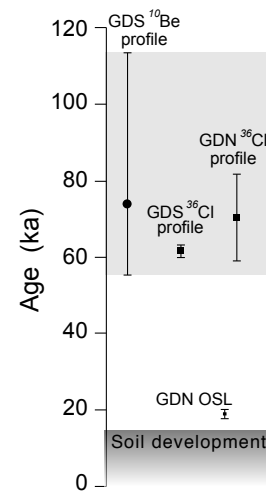


Figure 11. Summary of age results on displaced unit Qfi alluvial fan surface at sites GDN and GDS (Gumdrop Hills fault; Fig. 5). The terrestrial cosmogenic nuclide ^{10}Be and ^{36}Cl profiles and the optically stimulated luminescence (OSL) sample are plotted along with the associated uncertainties, represented by error bars. The range of cosmogenic ages is shaded in light gray. Cosmogenic profile models and pit characteristics are shown in Figures 8 and 9. Equivalent dose plot and age calculation of OSL is provided in Figure 10.

1985) (Table SB3 [footnote 1]). The elevated clay content and increased carbonate stage of this soil indicate that this surface is older than the soils observed in the site GDN and GDS pits and likely predates the Lahontan highstand (ca. 15.5 ka; e.g., Adams and Wesnousky, 1999). We interpret this surface to be >15.5 ka in age based on the soil.

The ¹⁰Be concentrations of six depth profile samples from the site Mina1-BS pit generally display a decrease in concentration with depth, with the exception of the sample at 30 cm depth (Fig. 8C). Modeling of the profile concentrations using the Hidy et al. (2010) modeler provides a most probable age of 21.7^{+10.8/-7.1} ka (Table 1). This age result is in general agreement with the interpretations based on the soil development and is interpreted here to represent the depositional age of the alluvial fan.

Site PS Pit (PSP1) and Surface Boulders

The PSP1 pit was emplaced on the unit Qfi surface into which the beheaded channel is incised at the PS site along the Petrified Springs fault (Fig. 7B). The alluvial fan surface sits ~2 m above the active alluvium and has a desert pavement scattered with varnished andesite boulders (Fig. 9C). The pit exposes a poorly sorted angular pebble to cobble conglomerate with a sandy matrix. A well-developed ~15-cm-thick rubified argillic Bt-horizon is present within the upper 25 cm of the deposit (Fig. 9C), with stage III carbonate development (Machette, 1985) below (Table SB3 [footnote 1]). The advanced soil development and elevated carbonate stage displayed in this pit suggest that this surface is the oldest of all of the sites. Prior observations of the soil at this site led Wesnousky (2005a) to correlate this surface to a 60–90 ka alluvial fan deposit within Bettles Well Canyon (Bell, 1995), located near the southern end of the Benton Springs fault (Fig. 2).

The ³⁶Cl concentrations of the six depth profile samples display a systematic decrease with depth (Fig. 9C). Modeling from CRONUScalc software (Marrero et al., 2016) depth profile appears to capture most of the data and provides a best-fit exposure age of 153.5 ± 11.2 ka (Table 2). Four andesite boulders were also sampled from the unit Qfi surface (PSB1–PSB4; Fig. 7B). Exposure age modeling using the CRONUScalc surface online calculator (Marrero et al., 2016) yields average age results of 127 ± 33, 305 ± 76, 119 ± 24.5, and 410 ± 150 ka for boulders PSB1, PSB2, PSB3, and PSB4, respectively (Table 3).

Comparison of the age results from the ³⁶Cl depth profile and surface boulders at site PS is shown in Figure 12. The range of age results spans 94 to 560 ka and shows two age populations: one between 94 and 165 ka, and the other from 229 to 560 ka (Fig. 12). The younger cluster (group 1 in Fig. 12), composed of two boulders and the depth profile, is more consistent with the presence of the Bt-horizon and stage III carbonate observed in the soil, whereas a much greater carbonate development (e.g., stage IV) would be expected for a soil approaching the age range of group 2 (Fig. 12) or surpassing 300 ka (e.g., Machette, 1985; Harden et al., 1991). On this basis, the older sample cluster, which is composed solely of surface boulder ages, is considered to contain

TABLE 3. ³⁶Cl BOULDER EXPOSURE AGE RESULTS AT SITE PS

³⁶ Cl boulder sample	Lifton et al. (2014) (ka)	Lal (1987), Stone (2000) (ka)	Average age (ka)
PSB1	116 ± 22	130 ± 30	127 ± 33
PSB2	276 ± 47	315 ± 66	305 ± 76
PSB3	111 ± 16	123 ± 21	119 ± 24.5
PSB4	370 ± 110	430 ± 130	410 ± 150

Notes: Ages calculated from the measured concentrations and parameters provided in Table SB2 (see text footnote 1) using CRONUScalc (Marrero et al., 2016). We use the average age using the scaling schemes of Lifton et al. (2014) and of Lal (1987) and Stone (2000). Bold indicates the age used for slip rate calculations.

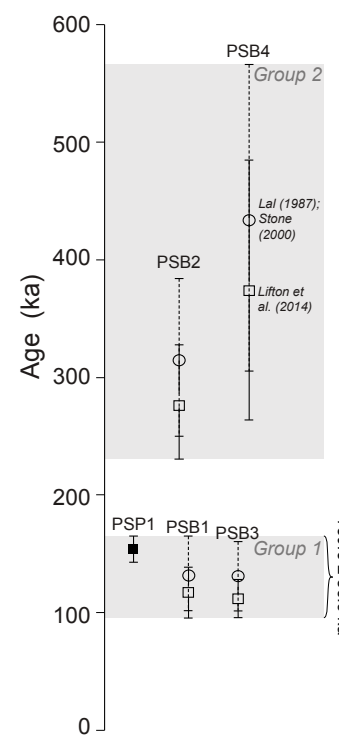


Figure 12. Summary of ³⁶Cl boulder and profile ages on the displaced alluvial fan at site PS on the Petrified Springs fault. Sample locations are shown in Figure 7B. The solid black square shows the most probable age result from the ³⁶Cl cosmogenic pit using CRONUScalc (Marrero et al., 2016). Boulder age results using the (Lifton et al., 2014) scaling scheme are shown as hollow squares with solid lines representing uncertainty, and hollow circles with dashed lines are results using the scaling scheme of Lal (1987) and Stone (2000). Light gray shading shows the age ranges of groups 1 and 2.

a significant inherited signal, and the younger population more likely to represent the depositional age of the unit Qfi alluvial fan surface. We interpret the average age of the younger cluster (130.8 ± 36.9 ka; Fig. 12) as the most representative of the age of abandonment of the alluvial fan, and this age is consistent with the observed degree of soil development.

■ SLIP RATES

Fault slip rates are calculated by dividing the measured offsets by the estimated age of the offset surface at each site. The rate estimates calculated in this manner are formalized using the probabilistic approach of Zechar and Frankel (2009), where a probability distribution function (pdf) of the slip rate is solved from integration of the age and displacement pdfs. The slip-rate results, along with values of offset and age that are at the 95% confidence level and used for the calculations, are listed in Table 4, and plots of the pdf of the slip rate for each site are provided in Figure 13. The rates determined at each site are considered to be minimum rates, due to the assumption that the measured displacements accrued sometime after the alluvial fan surfaces were abandoned. The slip rates estimated here are based on measurements collected at single sites along each the four faults, and therefore there is some additional uncertainty in the estimation of rates for the entire fault, related to the site location. For example, the slip rate sites on the Gumdrop Hills fault (sites GDN and GDS) and Benton Springs fault (site Mina1-BS) are located at the southern ends of each of the faults (Fig. 2), and it is possible that the measured offsets may underrepresent the total amount of slip on each fault (e.g., Bürgmann et al., 1994; Jonsson et al., 2002), thus the slip rate estimates from this study may underestimate the actual rate for the Gumdrop Hills and Benton Springs faults.

Indian Head Fault

The slip rate on the Indian Head fault site is determined by dividing the measured 8 ± 0.8 m offset fan terrace riser at site IH (Figs. 4B and 4C) by the lower end of the age result (10.3 ± 0.5 ka) provided by the ^{10}Be profile of the site IH pit (Fig. 8A), yielding a minimum slip rate of 0.8 ± 0.1 mm/yr (Fig. 13). This is the shortest-term geologic rate, averaged over the Holocene, of the central Walker Lane faults.

Gumdrop Hills Fault

The slip rate for the Gumdrop Hills fault is determined by dividing the cumulative right-lateral displacement of 17.1 ± 4.1 m measured between the two offset alluvial fan terrace risers at sites GDN and GDS (Figs. 5B and 5C) by the 18.9 ± 2.4 ka age result provided by the OSL sample collected within the site GDN pit (Fig. 10). The OSL age places a maximum age bound to the displaced surface, yielding a minimum Late Pleistocene slip rate of $0.9^{+0.3}/_{-0.2}$ mm/yr for the Gumdrop Hills fault (Fig. 13).

Benton Springs Fault

The Benton Springs fault slip rate is derived by dividing the 34.5 ± 2.8 m of displacement measured within the unit Qf1 alluvial fan terrace riser (Fig. 6B) by

TABLE 4. RESULTS OF SLIP RATE ANALYSIS

Fault	Site	Right-lateral displacement (m)	Age (ka)	Slip rate (mm/yr)
Indian Head fault	IH	8 ± 0.8	10.3 ± 0.5	0.8 ± 0.1
Gumdrop Hills fault	GDN, GDS	17.3 ± 4.1	18.9 ± 2.4	$0.9^{+0.3}/_{-0.2}$
Benton Springs fault	Mina1-BS	34.5 ± 2.8	$21.8^{+4.1}/_{-0.6}$	1.5 ± 0.2
Petrified Springs fault	PS	92.5 ± 5	124 ± 6	$0.7^{+0.3}/_{-0.2}$

Notes: Slip rate analyzed by using the probabilistic approach of Zechar and Frankel (2009) and applying Gaussian probability distribution functions to represent the measures of displacement and age results determined at each site. The uncertainties associated with the slip rate results are presented at 95% confidence level.

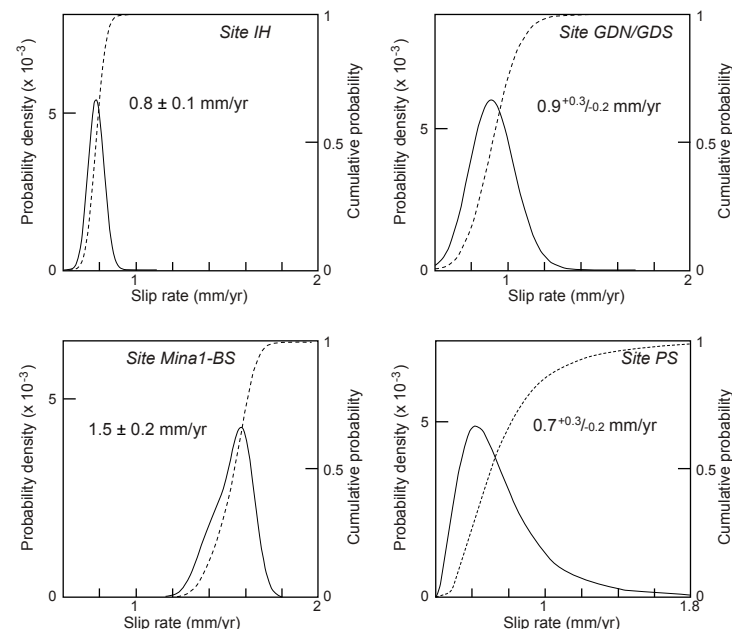


Figure 13. Horizontal slip rate probability density functions (PDFs) using the Zechar and Frankel (2009) method based on measured offset risers and modeled ages of each slip rate site (IH—Indian Head fault; GDN, GDS—Gumdrop Hills fault; Mina1-BS—Benton Springs fault; PS—Petrified Springs fault). Input parameters are provided in Table 4. Solid black line represents the PDF of the slip rate, and the dashed line represents the cumulative probability distribution.

the ^{10}Be depth profile age result ($21.8^{+4.1}/_{-0.6}$ ka) obtained in the site Mina1-BS pit (Fig. 8C), yielding a minimum Late Pleistocene slip rate of 1.5 ± 0.2 mm/yr (Fig. 13). This is the highest rate of all of the central Walker Lane faults and supports prior estimates of >1 mm/yr based on soil chronosequences (Wesnousky, 2005a).

Petrified Springs Fault

The slip rate determined at site PS on the Petrified Springs fault is calculated by combining the 92.5 ± 0.5 m of right-lateral offset on the beheaded channel (Fig. 7C) with the younger age group range of 124 ± 6 ka, established by the ^{36}Cl TCN analysis (Fig. 12). This yields a minimum Late Pleistocene slip rate of $0.7^{+0.3}/_{-0.2}$ mm/yr (Fig. 13). This rate is lower than prior geologic estimates (1.1–1.7 mm/yr; Wesnousky, 2005a), which were based on similar geomorphic relationships at this same site (Fig. 7C). The rate discrepancy is largely attributed to differences in the age assigned to the unit Qfi alluvial fan surface into which the beheaded channel is incised, placing a maximum age on the measured offset (Fig. 7C). The Wesnousky (2005a) study relied on the soil characteristics within the site PS pit and regional age correlations, whereas this study places an absolute age based on TCN measurements on the unit Qfi alluvial fan, offering a more direct measure of the age of the unit Qfi alluvial fan at the Petrified Springs site (Fig. 7C). On this basis, we infer the rate from this study ($0.7^{+0.3}/_{-0.2}$ mm/yr) to best define the Late Pleistocene slip rate for the Petrified Springs fault.

DISCUSSION

The new measures of offset and the application of numerical dating techniques to the respective offset surfaces has yielded both new and revised Holocene to Late Pleistocene minimum slip rates for the Petrified Springs ($0.7^{+0.3}/_{-0.2}$ mm/yr), Benton Springs (1.5 ± 0.2 mm/yr), Indian Head (0.8 ± 0.1 mm/yr), and Gumdrop Hills ($0.9^{+0.3}/_{-0.2}$ mm/yr) faults. The rates, measures of offset, and characteristics of the fault traces provide a basis to discuss the characteristics of earthquake recurrence, the spatial and temporal history of late Quaternary displacement on the fault system, and compare the amount of observed geodetic slip with what is now geologically accounted for by the central Walker Lane strike-slip faults. As well, they provide a basis to illustrate the importance of complementing TCN and OSL measurements of fan age with observations of soil development.

Surface Rupture Characteristics and Implication for Holocene Earthquakes

The measured offsets and mapped traces of the central Walker Lane strike-slip faults within Holocene deposits (unit Qfy; Figs. 2 and 3) provide insight to the recent rupture characteristics. Application of empirical scaling relationships between earthquake rupture length and displacement indicates that rupture of the entire ~40-km-long Holocene trace of the Indian Head fault would produce a coseismic slip of 1–3 m with an associated $M_w \sim 6.8$ earthquake (Wells and Coppersmith, 1994; Wesnousky, 2008). On this basis, it would be suggested that the ~8 m of measured right-lateral displacement at site IH (Fig. 4B) is

likely the result of at least two, and possibly three, surface-rupturing events in the Holocene. Dividing the 1–3 m offset by the 0.8 ± 0.1 mm/yr slip rate estimated for the fault in this study yields an expected recurrence interval for similar-size ruptures of ~3000–4000 yr. When taking the same approach for the ~35-km-long Holocene trace of the southern Benton Springs fault, it would be expected for coseismic displacements to be on the order of 1–3 m, also with an associated $M_w \sim 6.8$ earthquake. The 3 m right-lateral offset observed along the Holocene trace (Fig. 3A) is in the range of expected coseismic displacements and likely representative of the most recent surface-rupturing earthquake, occurring ca. 800 ^{14}C yr B.P. (Wesnousky, 2005a). Dividing the 3 m offset by the new slip rate determined for the Benton Springs fault (1.5 ± 0.2 mm/yr) provides a recurrence interval of similar-size ruptures of 1600–2300 yr.

The observations suggest that the Indian Head fault has ruptured several times during the Holocene. Because the slip rates of the other faults, excluding the Benton Springs fault, are similar to that of the Indian Head fault, it can also be expected that they have also ruptured at least once during the Holocene.

Late Quaternary Spatial and Temporal Distribution of Slip

Spatial and temporal variations of fault slip rates and return times are common within generally younger and less-developed fault systems (e.g., Cowie and Roberts, 2001), such as the Walker Lane (Wesnousky, 2005b; Faulds and Henry, 2008). In the southern Walker Lane in California, spatial and temporal variability of late Quaternary slip and the rate of slip has been reported along the Death Valley–Fish Lake Valley fault system (Frankel et al., 2007a, 2007b, 2011; Fig. 1) as well as the Owens Valley–White Mountain fault system (Kirby et al., 2006; Kirby et al., 2008; Fig. 1). Similarly, late Quaternary variations of slip rate have been observed on the Warm Springs fault (California) (Gold et al., 2013; Fig. 1) in the northern portion of the Walker Lane and attributed to transfer of slip back and forth between the Warm Springs fault and Honey Lake fault system (Fig. 1). The temporal and spatial variations in fault slip rate in each of these instances are attributed by the authors of the studies to the temporal transference of slip accommodation between proximal and subparallel faults. The slip history we observe along the central Walker Lane faults is consistent with this idea.

The Quaternary mapping show each of the central Walker Lane strike-slip faults to have been active during the Late Pleistocene, evidenced by mapped fault scarps within Late Pleistocene alluvial fans (unit Qfi) (Fig. 2). The Indian Head and southern Benton Springs faults, however, are the only two fault strands displaying unequivocal Holocene activity (Figs. 2 and 3). This would suggest that only two of the five central Walker Lane strike-slip faults have been accommodating strain during the Holocene. The absence of observed Holocene faulting along the Gumdrop Hills, Petrified Springs, northern Benton Springs, and Agai Pah fault traces may be attributed to longer recurrence intervals; however, as pointed out in the discussion section above, the faults share similar slip rates and, on that basis, it would be expected that each exhibit at

least one episode of Holocene displacement. These observations infer that slip rates on the central Walker Lane strike-slip faults are susceptible to vary over the short term (<10,000 yr).

Comparing Geologic and Geodetic Slip Rates

The measured values of offset versus the age of the offset feature at each slip rate site are plotted as small stars in Figure 14. The slopes of the lines define the average fault slip rate over the time since the respective offset surfaces were abandoned and extend through the time periods of which they are observed to be active based on the observations from the Quaternary mapping. At the top of the graph, we plot the cumulative geodetic strike-slip rate estimates for the central Walker Lane strike-slip faults. Summing of the rates for the faults determined to be active in the Holocene, the Benton Springs and Indian Head faults, yields a cumulative Holocene slip rate of 2.3 ± 0.3 mm/yr (Fig. 14). This rate appears to be consistent with the geodetic estimates, falling within the range of 0.9–3.2 mm/yr (Fig. 14; Bormann et al., 2016), and further supports our interpretations of the rupture recency based on Quaternary mapping. The sum of the newly determined Late Pleistocene slip rates found for the Benton Springs, Gumdrop Hills, and Petrified Springs faults yields a cumulative rate of 3.2 ± 0.7 mm/yr (thick black line in Fig. 14). This rate appears to be at the highest end of the geodetic estimates (Fig. 14), and should be regarded as a minimum cumulative rate, as Late Pleistocene slip rates for the Indian Head and Agai Pah fault remain undetermined. Provided that these two faults also displace Late Pleistocene alluvial fans (unit Qf; Fig. 2), it is likely the cumulative Late Pleistocene rate for all of the central Walker Lane strike-slip faults would exceed the geodetic range, allowing the interpretation that the amount of slip accommodated by the central Walker Lane strike-slip fault system may have decreased since the Late Pleistocene.

This comparison between the geodetic and new geologic rates along with the observations from the Quaternary mapping are consistent with the slip calculations of Bormann et al. (2016), and indicate that the geodetically determined rate of dextral slip across the central Walker Lane strike-slip fault system has likely been accomplished by only two of the five major strike-slip faults during the Holocene. It appears that the strike-slip faults have accommodated about one-third of the ~8 mm/yr of deformation geodetically measured across the central portion of the Walker Lane during the Holocene, and possibly one-half of the budget during the Late Pleistocene. Consequently, the remainder of the deformation budget is occurring to the southwest, where dextral shear strain is accommodated in the absence of strike-slip faults (Fig. 1). Here, paleomagnetic measurements of late Miocene volcanic rocks by Carlson et al. (2013) show the region to be dominated by vertical-axis block rotations within the Bodie Hills and Sweetwater Mountains in California that are associated with normal and left-lateral faults (Fig. 1). The calculated rates of Bormann et al. (2016) suggest relatively higher rates of block rotation and both extension and shear along the basin-bounding faults (e.g., Mono Lake fault and Silver Lake

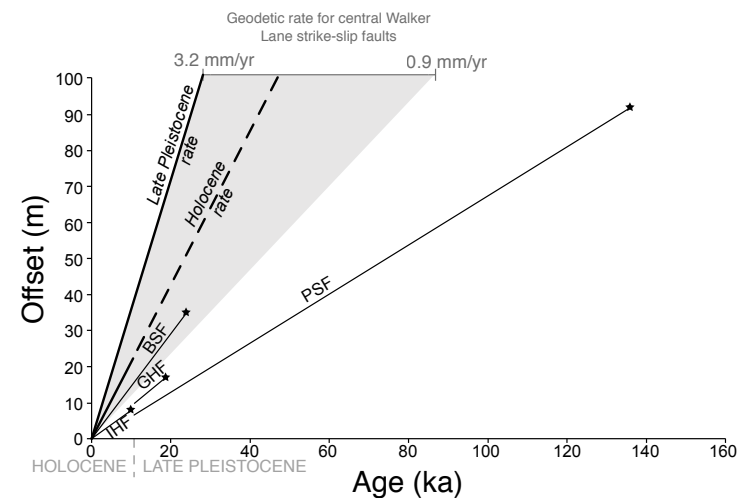


Figure 14. Summary of slip rates and recency of surface rupture. Stars show age result and offset measurement for each slip rate site. The slopes of lines represent the fault slip rate averaged over the age of the displacement for the Petrified Springs fault (PSF, $0.7^{+0.3/-0.2}$ mm/yr), Benton Springs fault (BSF, 1.5 ± 0.2 mm/yr), Indian Head fault (IHF, 0.8 ± 0.1 mm/yr), and Gumdrop Hills fault (GHF, $0.9^{+0.3/-0.2}$ mm/yr). The slip rates are plotted over the time span for which the faults have been found to have been active based on Quaternary mapping results. Thick lines represent cumulative Late Pleistocene rates (solid) and those determined to be active in the Holocene (dashed). Range of geodetically determined rates is shown with gray shading (Bormann et al., 2016).

fault, California; Fig. 1), and the observations from this study would support these predictions.

In sum, it appears that dextral shear has been more or less equally distributed across the central Walker Lane throughout the late Quaternary and that the locus of slip temporally transfers within the system of strike-slip faults of this study. This pattern of equally distributed and temporally variable strain release may be common throughout the Walker Lane (e.g., Frankel et al., 2011; Gold et al., 2014). The Walker Lane has been interpreted as an incipient plate boundary (Faulds et al., 2005), and shown to be relatively structurally complex when compared to the San Andreas (Wesnousky, 2005b), the main plate boundary fault between North America and the Pacific plate (Fig. 1). It could thus be inferred that as deformation accrues in the Walker Lane, structural maturity will result in a more organized linear zone of focused dextral shear within the central Walker Lane (Wesnousky, 1988).

Utility of Soil Development in Interpreting TCN Age Results

The uncertainties associated with age results from numerical dating techniques, such as TCN dating, frequently can be derived from the assumptions needed for age calculation, such as erosion rates (Anderson et al., 1996; Gosse

and Phillips, 2001; Hidy et al., 2010; Marrero et al., 2016). Soil development analysis also has uncertainty, but provides an independent measure of relative age for geomorphic surfaces, and in this study, served to be advantageous where the numerical dating techniques yielded conflicting or bimodal ages. For example, the relatively weak soil development observed in both the site GDN and GDS pits (Figs. 9A and 9B; Table SB3 [footnote 1]) along the Gumdrop Hills fault called into question the relatively consistent older TCN results from both pits. The older ages obtained through TCN analysis for the sites GDN and GDS are likely to be associated with a higher inheritance than quantified in the models, possibly the result of limitations of input assumptions needed for the model algorithms or additional surfaces processes not recognized in the scope of this study. Because the surface had no boulders or pebbles available that are suitable for cosmogenic analysis, it was not possible to cross-correlate the two TCN techniques, like the case of the PSP surface. The corroborating result of the OSL sample with the inferred soil age guided our age interpretation for the surface age at both sites of the offset alluvial fan (Fig. 11).

Similarly, the advanced stages of carbonate development and pedogenesis observed in the PSP1 pit at site PS (Fig. 9C; Table SB3 [footnote 1]) supported the relatively older ^{36}Cl TCN age results and guided our choice amongst the two age populations (Fig. 12). Finally, the pedogenic properties of the offset alluvial fan deposits along the Indian Head and Benton Springs faults also supported the TCN age results at the site IH pit (Fig. 8A; Table SB3 [footnote 1]) and at the site Mina1-BS pit (Fig. 8C; Table SB3 [footnote 1]), respectively. The examples from this study illustrate the utility of soils as a means of comparison, and that such a comparison should be considered as a requisite internal consistency check in the evaluation of TCN surface exposure ages.

CONCLUSIONS

New offset measurements and the application of numerical dating techniques of displaced alluvial fan surfaces place new minimum late Quaternary dextral strike-slip rates on the Benton Springs (1.5 ± 0.2 mm/yr), Petrified Springs ($0.7^{+0.3}_{-0.2}$ mm/yr), Gumdrop Hills ($0.9^{+0.3}_{-0.2}$ mm/yr), and Indian Head (0.8 ± 0.1 mm/yr) faults of the central Walker Lane. The sum of slip rates is across this portion of the Walker Lane is generally consistent with that reported by others from geodesy. Regional Quaternary mapping of the central Walker Lane strike-slip faults, however, shows that the southern segment of the Benton Springs and Indian Head faults have likely had multi-event Holocene ruptures with estimated maximum magnitudes on the order of $M_w \sim 6.8$ and associated coseismic horizontal displacements in the range 1–3 m, while surface rupture on the Gumdrop Hills and Petrified Springs faults have likely not occurred since the Late Pleistocene. In this regard, geology shows that the geodetically registered slip was relatively evenly divided among the four faults of the central Walker Lane during the Late Pleistocene, but has been focused on just two during the Holocene. The results thus provide an example of the temporal transfer of the locus of slip across closely spaced strike-slip

fault systems, a phenomenon that cannot be recognized by geodesy alone. Finally, the observation of profiles of soil development should be considered a requisite internal consistency check in the evaluation of TCN surface exposure ages used for the assessment of fault slip rates.

ACKNOWLEDGMENTS

This research was supported in part by National Science Foundation grants EAR-1419724 and EAR-1419789. We thank the two anonymous reviewers who provided thoughtful feedback that improved the paper. Visiting graduate student Xinnan Li from the China Earthquake Administration provided great assistance toward hand-digging many of the pits, documentation of soil characteristics, and careful sampling for cosmogenics. Many thanks to Jason Cesta who provided essential advice and assistance for the cosmogenic ^{36}Cl sample preparation and age modeling. Useful discussions in the field and at the office with Chad Carlson, Bill Hammond, Jayne Bormann, Ian Pierce, and Tabor Reedy provided valuable insight to this study. This is University of Nevada, Reno, Center for Neotectonic Studies contribution number 77.

REFERENCES CITED

- Adams, K.D., and Wesnousky, S.G., 1999, The Lake Lahontan highstand: Age, surficial characteristics, soil development, and regional shoreline correlation: *Geomorphology*, v. 30, p. 357–392, [https://doi.org/10.1016/S0169-555X\(99\)00031-8](https://doi.org/10.1016/S0169-555X(99)00031-8).
- Anderson, R.S., Repka, J.L., and Dick, G.S., 1996, Explicit treatment of inheritance in dating depositional surfaces using in situ ^{10}Be and ^{26}Al : *Geology*, v. 24, p. 47–51, [https://doi.org/10.1130/0091-7613\(1996\)024<0047:ETOIDD>2.3.CO;2](https://doi.org/10.1130/0091-7613(1996)024<0047:ETOIDD>2.3.CO;2).
- Angster, S., Wesnousky, S., Huang, W.L., Kent, G., Nakata, T., and Goto, H., 2016, Application of UAV photography to refining the slip rate on the Pyramid Lake fault zone, Nevada: *Bulletin of the Seismological Society of America*, v. 106, p. 785–798, <https://doi.org/10.1785/0120150144>.
- Bachman, G.O., and Machette, M.N., 1977, Calcic soils and calcretes in the southwestern United States: U.S. Geological Survey Open File Report 77-794, 163 p., <https://doi.org/10.3133/ofr77794>.
- Bell, J.W., 1995, Quaternary geologic map of the Mina quadrangle, Nevada: Nevada Bureau of Mines and Geology Field Studies Map 10, scale 1:24,000.
- Bell, J.W., Caskey, S.J., Ramelli, A.R., and Guerrieri, L., 2004, Pattern and rates of faulting in the central Nevada seismic belt, and paleoseismic evidence for prior beltlike behavior: *Bulletin of the Seismological Society of America*, v. 94, p. 1229–1254, <https://doi.org/10.1785/0120032226>.
- Bennett, R.A., Friedrich, A.M., and Furlong, K.P., 2004, Codependent histories of the San Andreas and San Jacinto fault zones from inversion of fault displacement rates: *Geology*, v. 32, p. 961–964, <https://doi.org/10.1130/G20806.1>.
- Benson, L.V., 1978, Fluctuations in the level of pluvial Lake Lahontan during the last 40,000 years: *Quaternary Research*, v. 9, p. 300–318, [https://doi.org/10.1016/0033-5894\(78\)90035-2](https://doi.org/10.1016/0033-5894(78)90035-2).
- Birkeland, P.W., 1984, *Soils and Geomorphology*: New York, Oxford University Press, 372 p.
- Bormann, J.M., Hammond, W.C., Kreemer, C., and Blewitt, G., 2016, Accommodation of missing shear strain in the Central Walker Lane, western North America: Constraints from dense GPS measurements: *Earth and Planetary Science Letters*, v. 440, p. 169–177, <https://doi.org/10.1016/j.epsl.2016.01.015>.
- Bull, W.B., 2008, *Tectonic Geomorphology of Mountains: A New Approach to Paleoseismology*: John Wiley & Sons, 328 p.
- Burbank, D.W., and Anderson, R.S., 2012, *Tectonic Geomorphology* (2nd edition): Oxford, UK, Blackwell Publishing Ltd., 453 p.
- Bürgmann, R., Pollard, D.D., and Martel, S.J., 1994, Slip distributions on faults: Effects of stress gradients, inelastic deformation, heterogeneous host-rock stiffness, and fault interaction: *Journal of Structural Geology*, v. 16, p. 1675–1690, [https://doi.org/10.1016/0191-8141\(94\)90134-1](https://doi.org/10.1016/0191-8141(94)90134-1).
- Carlson, C.W., 2014, Preliminary geologic map of the Terrill Mountains quadrangle, Churchill and Mineral Counties, Nevada: Nevada Bureau of Mines and Geology Open-File Report 2014-04, scale 1:24,000.
- Carlson, C.W., Pluhar, C.J., Glen, J.M.G., and Farner, M.J., 2013, Kinematics of the west-central Walker Lane: Spatially and temporally variable rotations evident in the Late Miocene Stanislaus Group: *Geosphere*, v. 9, p. 1530–1551, <https://doi.org/10.1130/GES00955.1>.

- Cashman, P.H., and Fontaine, S.A., 2000, Strain partitioning in the northern Walker Lane, western Nevada and northeastern California: *Tectonophysics*, v. 326, p. 111–130, [https://doi.org/10.1016/S0040-1951\(00\)00149-9](https://doi.org/10.1016/S0040-1951(00)00149-9).
- Cowie, P.A., and Roberts, G.P., 2001, Constraining slip rates and spacings for active normal faults: *Journal of Structural Geology*, v. 23, p. 1901–1915, [https://doi.org/10.1016/S0191-8141\(01\)00036-0](https://doi.org/10.1016/S0191-8141(01)00036-0).
- Dokka, R.K., and Travis, C.J., 1990, Role of the eastern California shear zone in accommodating Pacific–North American plate motion: *Geophysical Research Letters*, v. 17, p. 1323–1326, <https://doi.org/10.1029/GL017i009p01323>.
- Dolan, J.F., McAuliffe, L.J., Rhodes, E.J., McGill, S.F., and Zinke, R., 2016, Extreme multi-millennial slip rate variations on the Garlock fault, California: Strain super-cycles, potentially time-variable fault strength, and implications for system-level earthquake occurrence: *Earth and Planetary Science Letters*, v. 446, p. 123–136, <https://doi.org/10.1016/j.epsl.2016.04.011>.
- Dong, S., Ucakus, G., Wesnousky, S.G., Maloney, J., Kent, G., Driscoll, N. and Baskin, R., 2014, Strike-slip faulting along the Wassuk Range of the northern Walker Lane, Nevada: *Geosphere*, v. 10, p. 40–48, <https://doi.org/10.1130/GES00912.1>.
- Ekren, E.B., and Byers, F.M., Jr., 1984, The Gabbs Valley Range—A well-exposed segment of the Walker Lane in west-central Nevada, in Lintz, J., Jr., ed., *Western Geological Excursions: Reno, Nevada*, University of Nevada Mackay School of Mines, Geological Society of America, Annual Meeting Guidebook, v. 4, p. 204–215.
- Ekren, E.B., and Byers, F.M., Jr., 1985a, Geologic map of the Gabbs Mountain, Mount Ferguson, Luning, and Sunrise Flat quadrangles, Mineral and Nye Counties, Nevada: U.S. Geological Survey Miscellaneous Investigations Map I-1577, scale 1:48,000, <https://doi.org/10.3133/i1577>.
- Ekren, E.B., and Byers, F.M., Jr., 1985b, Geologic map of the Win Wan Flat, Kinkaid NW, Kinkaid, and Indian Head Peak quadrangles, Mineral County, Nevada: U.S. Geological Survey Miscellaneous Investigations Map I-1578, scale 1:48,000, <https://doi.org/10.3133/i1578>.
- Ekren, E.B., and Byers, F.M., Jr., 1986a, Geologic map of the Mount Annie NE, Mount Annie, Ramsey Spring, and Mount Annie SE quadrangles, Mineral and Nye Counties, Nevada: U.S. Geological Survey Miscellaneous Investigations Map I-1579, scale 1:48,000, <https://doi.org/10.3133/i1579>.
- Ekren, E.B., and Byers, F.M., Jr., 1986b, Geologic map of the Murphys Well, Pilot Cone, Copper Mountain, and Poinsettia Spring quadrangles, Mineral County, Nevada: U.S. Geological Survey Miscellaneous Investigations Map I-1576, scale 1:48,000, <https://doi.org/10.3133/i1576>.
- Faulds, J.E., and Henry, C.D., 2008, Tectonic influences on the spatial and temporal evolution of the Walker Lane: An incipient transform fault along the evolving Pacific–North American plate boundary, in Spencer, J.E., and Tittley, S.R., eds., *Ores and Orogenesis: Circum-Pacific Tectonics, Geological Evolution, and Ore Deposits: Arizona Geological Society Digest 22*, p. 437–470.
- Faulds, J.E., Henry, C.D., and Hinz, N.H., 2005, Kinematics of the northern Walker Lane: An incipient transform fault along the Pacific–North American plate boundary: *Geology*, v. 33, p. 505–508, <https://doi.org/10.1130/G21274.1>.
- Frankel, K.L., Brantley, K.S., Dolan, J.F., Finkel, R.C., Klinger, R.E., Knott, J.R., Machette, M.N., Owen, L.A., Phillips, F.M., Slate, J.L., and Wernicke, B.P., 2007a, Cosmogenic ¹⁰Be and ³⁶Cl geochronology of offset alluvial fans along the northern Death Valley fault zone: Implications for transient strain in the eastern California shear zone: *Journal of Geophysical Research*, v. 112, B06407, <https://doi.org/10.1029/2006JB004350>.
- Frankel, K.L., Dolan, J.F., Finkel, R.C., Owen, L.A., and Hoeft, J.S., 2007b, Spatial variations in slip rate along the Death Valley–Fish Lake Valley fault system determined from LiDAR topographic data and cosmogenic ¹⁰Be geochronology: *Geophysical Research Letters*, v. 34, L18303, <https://doi.org/10.1029/2007GL030549>.
- Frankel, K.L., Dolan, J.F., Owen, L.A., Ganep, P. and Finkel, R.C., 2011, Spatial and temporal constancy of seismic strain release along an evolving segment of the Pacific–North America plate boundary: *Earth and Planetary Science Letters*, v. 304, p. 565–576, <https://doi.org/10.1016/j.epsl.2011.02.034>.
- Gold, R., dePolo, C., Briggs, R., Crone, A., and Gosse, J., 2013, Late Quaternary slip-rate variations along the Warm Springs Valley fault system, northern Walker Lane, California–Nevada border: *Bulletin of the Seismological Society of America*, v. 103, p. 542–558, <https://doi.org/10.1785/BSE2%80%8B0120120020>.
- Gold, R.D., Briggs, R.W., Personius, S.F., Crone, A.J., Mahan, S.A. and Angster, S.J., 2014, Latest Quaternary paleoseismology and evidence of distributed dextral shear along the Mohawk Valley fault zone, northern Walker Lane, California: *Journal of Geophysical Research: Solid Earth*, v. 119, p. 5014–5032, <https://doi.org/10.1002/2014JB010987>.
- Gosse, J.C., and Phillips, F.M., 2001, Terrestrial in situ cosmogenic nuclides: Theory and application: *Quaternary Science Reviews*, v. 20, p. 1475–1560, [https://doi.org/10.1016/S0277-3791\(00\)00171-2](https://doi.org/10.1016/S0277-3791(00)00171-2).
- Greene, R.C., Stewart, J.H., John, D.A., Hardyman, R.F., Silberling, N.J., and Sorensen, M.L., 1991, Geologic map of the Reno 1° by 2° quadrangle, Nevada and California: U.S. Geological Survey Miscellaneous Field Studies Map MF-2154-A, scale 1:250,000, <https://doi.org/10.3133/mf2154A>.
- Haddon, E.K., Amos, C.B., Zielke, O., Jayko, A.S., and Bürgmann, R., 2016, Surface slip during large Owens Valley earthquakes: *Geochemistry Geophysics Geosystems*, v. 17, p. 2239–2269, <https://doi.org/10.1002/2015GC006033>.
- Hammond, W.C., and Thatcher, W., 2004, Contemporary tectonic deformation of the Basin and Range province, western United States: 10 years of observation with the Global Positioning System: *Journal of Geophysical Research: Solid Earth*, v. 109, p. 1–21, <https://doi.org/10.1029/2003JB002746>.
- Hammond, W.C., Blewitt, G., and Kreemer, C., 2011, Block modeling of crustal deformation of the northern Walker Lane and Basin and Range from GPS velocities: *Journal of Geophysical Research*, v. 116, B04402, <https://doi.org/10.1029/2010JB007817>.
- Harden, J.W., Taylor, E.M., Hill, C., Mark, R.K., McFadden, L.D., Reheis, M.C., Sowers, J.M., and Wells, S.G., 1991, Rates of soil development from four soil chronosequences in the southern Great Basin: *Quaternary Research*, v. 35, p. 383–399, [https://doi.org/10.1016/0033-5894\(91\)90052-7](https://doi.org/10.1016/0033-5894(91)90052-7).
- Hardyman, R.F., 1980, Geology of the Gillis Canyon quadrangle, Mineral County, Nevada: U.S. Geological Survey Miscellaneous Investigations Map I-1237, scale 1:48,000, <https://doi.org/10.3133/i1237>.
- Hardyman, R.F., and Oldow, J.S., 1991, Tertiary tectonic framework and Cenozoic history of the central Walker Lane, Nevada, in Raines, G.L., Listle, R.E., Schafer, R.W., and Wilkinson, W.H., eds., *Geology and Ore Deposits of the Great Basin: Symposium Proceedings: Reno, Nevada*, Geological Society of Nevada, v. 1, p. 279–301.
- Hardyman, R.F., Ekren, E.B., and John, D.A., 2000, Evidence for Cenozoic dextral displacement across the Walker Lane, west central Nevada: *Geological Society of America Abstracts with Programs*, v. 32, no. 7, p. 105.
- Hidy, A.J., Gosse, J.C., Pederson, J.L., Mattern, J.P., and Finkel, R.C., 2010, A geologically constrained Monte Carlo approach to modeling exposure ages from profiles of cosmogenic nuclides: An example from Lees Ferry, Arizona: *Geochemistry, Geophysics, Geosystems*, v. 11, <https://doi.org/10.1029/2010GC003084>.
- Jonsson, S., Zebker, H., Segall, P., and Amelung, F., 2002, Fault slip distribution of the 1999 Mw 7.1 Hector Mine, California, earthquake, estimated from satellite radar and GPS measurements: *Bulletin of the Seismological Society of America*, v. 92, p. 1377–1389, <https://doi.org/10.1785/0120000922>.
- Kenner, S.J., and Simons, M., 2005, Temporal clustering of major earthquakes along individual faults due to post-seismic reloading: *Geophysical Journal International*, v. 160, p. 179–194, <https://doi.org/10.1111/j.1365-246X.2005.02460.x>.
- Kirby, E., Burbank, D.W., Reheis, M., and Phillips, F., 2006, Temporal variations in slip rate of the White Mountain Fault Zone, Eastern California: *Earth and Planetary Science Letters*, v. 248, no. 1–2, p. 168–185, <https://doi.org/10.1016/j.epsl.2006.05.026>.
- Kirby, E., Anandakrishnan, S., Phillips, F. and Marrero, S., 2008, Late Pleistocene slip rate along the Owens Valley fault, eastern California: *Geophysical Research Letters*, v. 35, <https://doi.org/10.1029/2007GL031970>.
- Koehler, R.D., and Wesnousky, S.G., 2011, Late Pleistocene regional extension rate derived from earthquake geology of late Quaternary faults across the Great Basin, Nevada, between 38.5°N and 40°N latitude: *Geological Society of America Bulletin*, v. 123, p. 631–650, <https://doi.org/10.1130/B30111.1>.
- Kreemer, C., Blewitt, G., and Hammond, W.C., 2009, Geodetic constraints on contemporary deformation in the northern Walker Lane: 2. Velocity and strain rate tensor analysis, in Oldow, J.S., and Cashman, P., eds., *Late Cenozoic Structure and Evolution of the Great Basin–Sierra Nevada Transition: Geological Society of America Special Paper 447*, p. 17–31, [https://doi.org/10.1130/2009.2447\(02\)](https://doi.org/10.1130/2009.2447(02)).
- Lal, D., 1987, Cosmogenic nuclides produced in situ in terrestrial solids: Nuclear Instruments and Methods in Physics Research Section B: Beam Interactions with Materials and Atoms, v. 29, p. 238–245, [https://doi.org/10.1016/0168-583X\(87\)90243-6](https://doi.org/10.1016/0168-583X(87)90243-6).
- Lee, J., Garwood, J., Stockli, D.F., and Gosse, J., 2009, Quaternary faulting in Queen Valley, California–Nevada: Implications for kinematics of fault-slip transfer in the eastern California shear zone–Walker Lane belt: *Geological Society of America Bulletin*, v. 121, p. 599–614, <https://doi.org/10.1130/B26352.1>.
- Li, X., Huang, W., Pierce, I.K., Angster, S.J., and Wesnousky, S.G., 2017, Characterizing the Quaternary expression of active faulting along the Olinghouse, Carson, and Wabuska lineaments of the Walker Lane: *Geosphere*, v. 13, p. 2119–2136, <https://doi.org/10.1130/GES01483.1>.

- Lifton, N.A., Sato, T., and Dunai, T.J., 2014, Scaling in situ cosmogenic nuclide production rates using analytical approximations to atmospheric cosmic-ray fluxes: *Earth and Planetary Science Letters*, v. 386, p. 149–160, <https://doi.org/10.1016/j.epsl.2013.10.052>.
- Loveless, J.P., and Meade, B.J., 2010, Geodetic imaging of plate motions, slip rates, and partitioning of deformation in Japan: *Journal of Geophysical Research*, v. 115, <https://doi.org/10.1029/2008JB006248>.
- Machette, M.N., 1985, Calcic soils of the southwestern United States, in Weide, D.L., ed., *Soils and Quaternary Geology of the Southwestern United States*: Geological Society of America Special Paper 203, p. 1–22, <https://doi.org/10.1130/SPE203-p1>.
- Marrero, S.M., Phillips, F.M., Borchers, B., Lifton, N., Aumer, R., and Balco, G., 2016, Cosmogenic nuclide systematics and the CRONUScal program: *Quaternary Geochronology*, v. 31, p. 160–187, <https://doi.org/10.1016/j.quageo.2015.09.005>.
- McCalpin, J.P., 2009, Application of paleoseismic data to seismic hazard assessment and neotectonic research, in McCalpin, J.P., ed., *Paleoseismology* (2nd edition): San Diego, California, Academic Press, [https://doi.org/10.1016/S0074-6142\(09\)95009-4](https://doi.org/10.1016/S0074-6142(09)95009-4).
- McFadden, L.D., McDonald, E.V., Wells, S.G., Anderson, K., Quade, J., and Forman, S.L., 1998, The vesicular layer and carbonate collars of desert soils and pavements: Formation, age and relation to climate change: *Geomorphology*, v. 24, p. 101–145, [https://doi.org/10.1016/S0169-555X\(97\)00095-0](https://doi.org/10.1016/S0169-555X(97)00095-0).
- Meade, B.J., and Hager, B.H., 2005, Block models of crustal motion in southern California constrained by GPS measurements: *Journal of Geophysical Research*, v. 110, B03403, <https://doi.org/10.1029/2004JB003209>.
- Oldow, J.S., Alken, C.L.V., Hare, J.L., Ferguson, J.F., and Hardyman, R.F., 2001, Active displacement transfer and differential block motion within the central Walker Lane, western Great Basin: *Geology*, v. 29, p. 19–22, [https://doi.org/10.1130/0091-7613\(2001\)029<0019:ADTADB>2.0.CO;2](https://doi.org/10.1130/0091-7613(2001)029<0019:ADTADB>2.0.CO;2).
- Owen, L.A., Frankel, K.L., Knott, J.R., Reynhout, S., Finkel, R.C., Dolan, J.F., and Lee, J., 2011, Beryllium-10 terrestrial cosmogenic nuclide surface exposure dating of Quaternary landforms in Death Valley: *Geomorphology*, v. 125, p. 541–557, <https://doi.org/10.1016/j.geomorph.2010.10.024>.
- Pérouse, E., and Wernicke, B., 2016, Spatiotemporal evolution of fault slip rates in deforming continents: The case of the Great Basin region, northern Basin and Range province: *Geosphere*, v. 13, p. 112–135, <https://doi.org/10.1130/GES01295.1>.
- Reheis, M.C., Shroba, R.R., Harden, J.W., and McFadden, L.D., 1989, Development rates of late Quaternary soils, Silver Lake Playa, California: *Soil Science Society of America Journal*, v. 53, p. 1127–1140, <https://doi.org/10.2136/sssaj1989.03615995005300040024x>.
- Rockwell, T.K., Lindvall, S., Herzberg, M., Murbach, D., Dawson, T., and Berger, G., 2000, Paleoseismology of the Johnson Valley, Kickapoo, and Homestead Valley faults: Clustering of earthquakes in the Eastern California shear zone: *Bulletin of the Seismological Society of America*, v. 90, p. 1200–1236, <https://doi.org/10.1785/0119990023>.
- Rogers, D.K., 1975, The Carson Lineament—Its influence on recent left-lateral faulting near Carson City, Nevada: *Geological Society of America Abstracts with Programs*, v. 7, no. 7, p. 1250.
- Sauber, J., Thatcher, W., Solomon, S.C., and Lisowski, M., 1994, Geodetic slip rate for the eastern California shear zone and the recurrence time of Mojave Desert earthquakes: *Nature*, v. 367, p. 264–266, <https://doi.org/10.1038/367264a0>.
- Soil Survey Division Staff, 1993, *Soil Survey Manual*: United States Department of Agriculture Handbook 18, 437 p.
- Stein, S., and Wysession, M., 2002, *An Introduction to Seismology, Earthquakes, and Earth Structure* (1st edition): Oxford, UK, Blackwell Publishing Ltd., 52 p.
- Stewart, J.H., 1988, Tectonics of the Walker Lane Belt, western Great Basin Mesozoic and Cenozoic deformation in a zone of shear, in Ernst, W.G., ed., *Metamorphism and Crustal Evolution of the Western U.S., Ruby Volume VII: Upper Saddle River, New Jersey, Prentice-Hall*, p. 685–713.
- Stone, J.O., 2000, Air pressure and cosmogenic isotope production: *Journal of Geophysical Research. Solid Earth*, v. 105, p. 23,753–23,759, <https://doi.org/10.1029/2000JB900181>.
- Thatcher, W., Foulger, G.R., Julian, B.R., Svarc, J., Quilty, E., and Bawden, G.W., 1999, Present-day deformation across the Basin and Range province, western United States: *Science*, v. 283, p. 1714–1718, <https://doi.org/10.1126/science.283.5408.1714>.
- Unruh, J., Humphrey, J., and Barron, A., 2003, Transtensional model for the Sierra Nevada frontal fault system, eastern California: *Geology*, v. 31, p. 327–330, [https://doi.org/10.1130/0091-7613\(2003\)031<0327:TMFTSN>2.0.CO;2](https://doi.org/10.1130/0091-7613(2003)031<0327:TMFTSN>2.0.CO;2).
- Vermeesch, P., 2009, RadialPlotter: A Java application for fission track, luminescence and other radial plots: *Radiation Measurements*, v. 44, p. 409–410, <https://doi.org/10.1016/j.radmeas.2009.05.003>.
- Wells, D.L., and Coppersmith, K.J., 1994, New empirical relationships among magnitude, rupture length, rupture width, rupture area, and surface displacement: *Bulletin of the Seismological Society of America*, v. 84, p. 974–1002.
- Wesnousky, S.G., 1988, Seismological and structural evolution of strike-slip faults: *Nature*, v. 335, p. 340–343, <https://doi.org/10.1038/335340a0>.
- Wesnousky, S.G., 2005a, Active faulting in the Walker Lane: *Tectonics*, v. 24, TC3009, <https://doi.org/10.1029/2004TC001645>.
- Wesnousky, S.G., 2005b, The San Andreas and Walker Lane fault systems, western North America: Transpression, transtension, cumulative slip and the structural evolution of a major transform plate boundary: *Journal of Structural Geology*, v. 27, p. 1505–1512, <https://doi.org/10.1016/j.jsg.2005.01.015>.
- Wesnousky, S.G., 2008, Displacement and geometrical characteristics of earthquake surface ruptures: Issues and implications for seismic-hazard analysis and the process of earthquake rupture: *Bulletin of the Seismological Society of America*, v. 98, p. 1609–1632, <https://doi.org/10.1785/0120070111>.
- Wesnousky, S.G., and Caffee, M.W., 2011, Range-bounding normal fault of Smith Valley, Nevada: Limits on age of last surface-rupture earthquake and late Pleistocene rate of displacement: *Bulletin of the Seismological Society of America*, v. 101, p. 1431–1437, <https://doi.org/10.1785/0120100238>.
- Wesnousky, S.G., Bormann, J.M., Kreemer, C., Hammond, W.C., and Brune, J.N., 2012, Neotectonics, geodesy, and seismic hazard in the Northern Walker Lane of Western North America: Thirty kilometers of crustal shear and no strike-slip?: *Earth and Planetary Science Letters*, v. 329–330, p. 133–140, <https://doi.org/10.1016/j.epsl.2012.02.018>.
- Youngs, R.R., and Coppersmith, K.J., 1985, Implications of fault slip rates and earthquake recurrence models to probabilistic seismic hazard estimates: *Bulletin of the Seismological Society of America*, v. 75, no. 4, p. 939–964.
- Zechar, J.D., and Frankel, K.L., 2009, Incorporating and reporting uncertainties in fault slip rates: *Journal of Geophysical Research*, v. 114, B12407, <https://doi.org/10.1029/2009JB006325>.
- Zielke, O., Klinger, Y., and Arrowsmith, R.J., 2012, LaDiCaoz and LiDARimager—MATLAB GUIs for LiDAR data handling and lateral displacement measurements: *Geosphere*, v. 8, no. 1, p. 206–221, <https://doi.org/10.1130/GES00686.1>.
- Zielke, O., Klinger, Y., and Arrowsmith, J.R., 2015, Fault slip and earthquake recurrence along strike-slip faults—Contributions of high-resolution geomorphic data: *Tectonophysics*, v. 638, p. 43–62, <https://doi.org/10.1016/j.tecto.2014.11.004>.